minerals

MDPI

Article

Comparative Study on Shale Characteristics of Different Sedimentary Microfacies of Late Permian Longtan Formation in Southwestern Guizhou, China

Xiao Ma [1,2] and Shaobin Guo [1,2,*]

[1] School of Energy Resources, China University of Geosciences (Beijing), Beijing 100083, China; mx1992cq@126.com

[2] Key Laboratory of Strategy Evaluation for Shale Gas, Ministry of Land and Resources, Beijing 100083, China

* Correspondence: guosb58@cugb.edu.cn; Tel.: +86-010-82326850

Received: 9 November 2018; Accepted: 22 December 2018; Published: 29 December 2018

Abstract: Organic-rich marine-continental transitional shales are widely distributed in Guizhou Province, China. Samples from the Late Permian Longtan Formation were investigated using organic petrography analysis, X-ray diffraction (XRD) analysis, field emission-scanning electron microscopy observations, mercury intrusion capillary pressure and gas adsorption experiments to better understand the organic geochemical characteristic, mineralogical composition, full-size pore structure characteristics and fractal characteristic of shale reservoir. The relationships among the total organic carbon (TOC) content, mineral composition, pore structure parameter, methane adsorption capacity and fractal dimension of shale samples are discussed, along with the differences between different sedimentary microfacies. Results show that shale samples are characterized by high TOC contents, low permeability, complex mineral composition and pore structure. Shales of YV-1, deposited in delta and lower delta plains, have an extreme high clay content (71.33% average) and the clay minerals mainly consist of the I/S and kaolinite, while shales of XD-1, deposited in the lagoon-tidal flat, have a relatively low clay content (37% average) and the I/S occupies an absolute advantage. The pore volume, specific surface area and average pore diameter of YV-1 (0.02881 cm^3/g, 20.806 m^2/g and 11.07 nm, respectively) are larger than that of XD-1 (0.02110 cm^3/g, 20.101 m^2/g, and 8.40 nm, respectively). The mesopore of YV-1 is the predominant contributor to the pore structure, while the micropore of XD-1 also occupies a certain proportion in addition to the mesopore. Organic matter (OM)-hosted pores are largely developed in XD-1 samples, while clay mineral-hosted pores dominate the pore system of YV-1. Shale samples with higher TOC content and clay content generally have larger specific surface area and pore volume, which provides more adsorption space and enhances pore structure heterogeneity. Samples of XD-1 have high TOC contents, suitable mineral composition and complex pore structure, suggesting that shales deposited in a lagoon-tidal flat environment may have a greater potential for shale gas development.

Keywords: Longtan formation shale; sedimentary microfacies; full-size pore structure; fractal characteristics; gas adsorption capacity

1. Introduction

The remarkable success in the commercial development of shale gas in North America has stimulated a shale gas exploration boom worldwide and significantly changed the pattern of global energy supplies. With the growth of energy demand and the improvement of experimental techniques, shale gas has attracted more attention and great progress has been made in China.

Previous studies have demonstrated that there are a large number of nano-scale pores and fractures in shale [1]. Production in low permeability shale critically depends on the nano-sized pore

systems for storing and releasing hydrocarbon gas. The pore geometry can be circular, ink-bottle shaped, wedge shaped or irregular shaped. Based on the genesis and position within the reservoir space, pores include organic pores, inorganic pores and fractures. According to the diameter, pores can be divided into three categories: micropores (diameter < 2 nm), mesopores (2 nm < diameter < 50 nm), and macropores (diameter > 50 nm) [2]. Organic-rich shale typically contains complex pore system, which is closely related to the multiple pore geometries, various pore types, and large pore size distribution. Thus, studies on pore system of shale reservoirs are essential to evaluating the gas storage-flow capacity and the production of shale gas wells [3].

Achievements in the testing methods in recent years provide a great opportunity to study the shale pore system. Qualitative analysis methods, including field emission-scanning electron microscopy (FE-SEM), nano-scale computed tomography (CT) scan and ultra small angle neutron scattering, are used to observe pore type and pore geometry, and measure pore size of shale [4–7]. Quantitative analysis methods, including mercury intrusion capillary pressure (MICP) and low-pressure gas adsorption, are usually used to calculate pore volume (PV) and specific surface area (SSA), and characterize pore size distribution (PSD) [8–10]. Moreover, the heterogeneity of shale pores can be quantitatively described by fractal theory [11]. The fractal dimension (D), obtained from nitrogen adsorption analysis using the fractal Frenkel–Halsey–Hill (FHH) model, has been proved to be an effective index to investigate surface roughness or structural irregularity of the pore [12] and has been reported in many research works [13,14].

The geochemical characteristics of shale also play an important role in the formation and accumulation of shale gas. Higher total organic carbon (TOC) content and appropriate thermal maturity are the key to the generation of hydrocarbon. Mineral composition and content, especially clay minerals and brittle minerals, have great influence on gas adsorption and fracturing [15].

In China, organic-rich shales are widely deposited in marine, terrestrial and marine-terrestrial transitional environments, showing big differences in geochemical features, reservoir performances, and have gas-bearing properties [16–18]. Compared with continental shale and marine-continental transitional shale, marine shale has greater potential for shale gas exploration because of its high TOC content, appropriate thermal maturity and favorable lithologic association. At present, significant breakthroughs have been achieved in terrestrial shale in northwestern China and marine shale in South China [19–22]. Although the marine-continental transitional shale in China has attracted more attention in recent years, research on shale reservoir characteristics is still relatively scarce. Comparative studies on the pore structure of marine, terrestrial, and transitional shales in key areas have been involved, while the comparative study on pore structure of transitional shales with different sedimentary facies remains to be conducted.

Shales of Late Permian Longtan Formation in Guizhou Province were deposited in a typical marine-continental transitional environment and found in coal-bearing strata, exhibiting high organic content, high maturity and a relatively large cumulative thickness [23,24]. In recent years, many mining areas and oil fields have been discovered. Take the Xiye-1 well and the Xingye-1 well as an example; in the drilling process, the gas content of the Xiye-1 ranges from 1.4 to 19.6 m^3/t, and the gas content of the Xingye-1 ranges from 1.2 to 4.2 m^3/t. This indicates that the marine-continental transitional Longtan shale has great potential for shale gas exploration, and that different sedimentary microfacies have an important influence on the gas-bearing property. Nevertheless, previous studies in this area are mainly concentrated in coal-bearing strata rather than shale gas.

The purpose of this article is to make a comparative study on geochemical characteristic, mineralogical composition and pore structure of shales with different sedimentary microfacies in typical areas of Guizhou. The effects of sedimentary facies on the gas-bearing property are also discussed. We use the analysis of total organic carbon, kergon type and X-ray diffraction (XRD) to determine the geochemical and mineralogy characteristics, and use MICP, low-pressure gas adsorption, scanning electron microscopy (SEM) and fractal theory to characterize the pore systems. Furthermore,

this study might provide some references for the evaluation of marine-continental transitional shale reservoirs with different sedimentary microfacies backgrounds in China.

2. Geological Background

Guizhou Province is located in the southeast margin of the upper Yangtze plate. Previous study [25] shows the Longtan shale in the southern Guizhou is characterized by high TOC content, high thermal maturity, great thickness and wide distribution. The geological backgrounds and geological attributes of transitional shales in this area are shown in Table 1. Shales with different sedimentary microfacies in the two promising exploration areas were selected as the study objects. The location of Panxian County and Xingren County is shown in Figure 1a. Many mine wells existed in Panxian County can help to investigate pore system of the transitional shale.

Table 1. Basic geological parameters of shale reservoirs in southwest Guizhou, cited from Guo et al. [25].

Stratum	Cumulative Thickness of Shale (m)	Total Organic Carbon (TOC) (wt.%)	R_o (%)	Kerogen Type	Brittle Mineral Content (wt.%)	Clay Mineral Content (wt.%)	Porosity (%)
Longtan Formation	10–50	0.53–17.3/6.07	1.57–2.66/2.45	III	47.8	41.4	0.2–11.1/2.5

Tectonically, Guizhou Province can be subdivided into six major structural units: north of the Yunnan-Guizhou depression, the Wuling depression, the central Guizhou uplift, the southwestern Guizhou depression, the southern Guizhou depression and the Xuefeng uplift [26]. Both of the two study areas are located in southwestern Guizhou depression (Figure 1a). The main tectonic evolution in Western Guizhou Province includes: a basement formation stage during the Wuling-Xuefeng period, a passive continental margin-stable platform stage during the Caledonian period, an intra-continental rifting-platform stage during the Hercynian period, a stable platform stage during the Indosinian period, and intra-continental river deposition stage during the Yanshan period and an overall uplift of mountain fault depression stage during the Himalayan period [27].

The superposition of multistage tectonic movement formed trough-like folds and different trending faults. The single fold is often S-shaped or anti S-shaped, indicating that the tectonic deformation was dominated by compression. Different trending faults may intersect each other. Panxian County is located in a coal-accumulated basin, which has a complex anticline and syncline structure and is restricted by the well-developed normal faults in the Panxian structural belt (Figure 1b) [28]. Peat-accumulation took place during Upper Permian have a complex process, the western flank of Panguan syncline first experienced uplift and denudation, and then sedimentary burial, which is favorable for shale gas reservoir preservation. In Xingren County, the folds are mainly NW trending, the axis is nearly upright, and the hinge zone of fold is smooth. The NE strike-slip faults are well developed, extending for tens of kilometers, and the fault spacing can reach hundreds of meters. The folds are often cut into several sections (Figure 1c). Most of the Late Permian coal-bearing strata are preserved in smooth synclines. The development of faults damaged the continuity and structural integrity of coal-bearing strata.

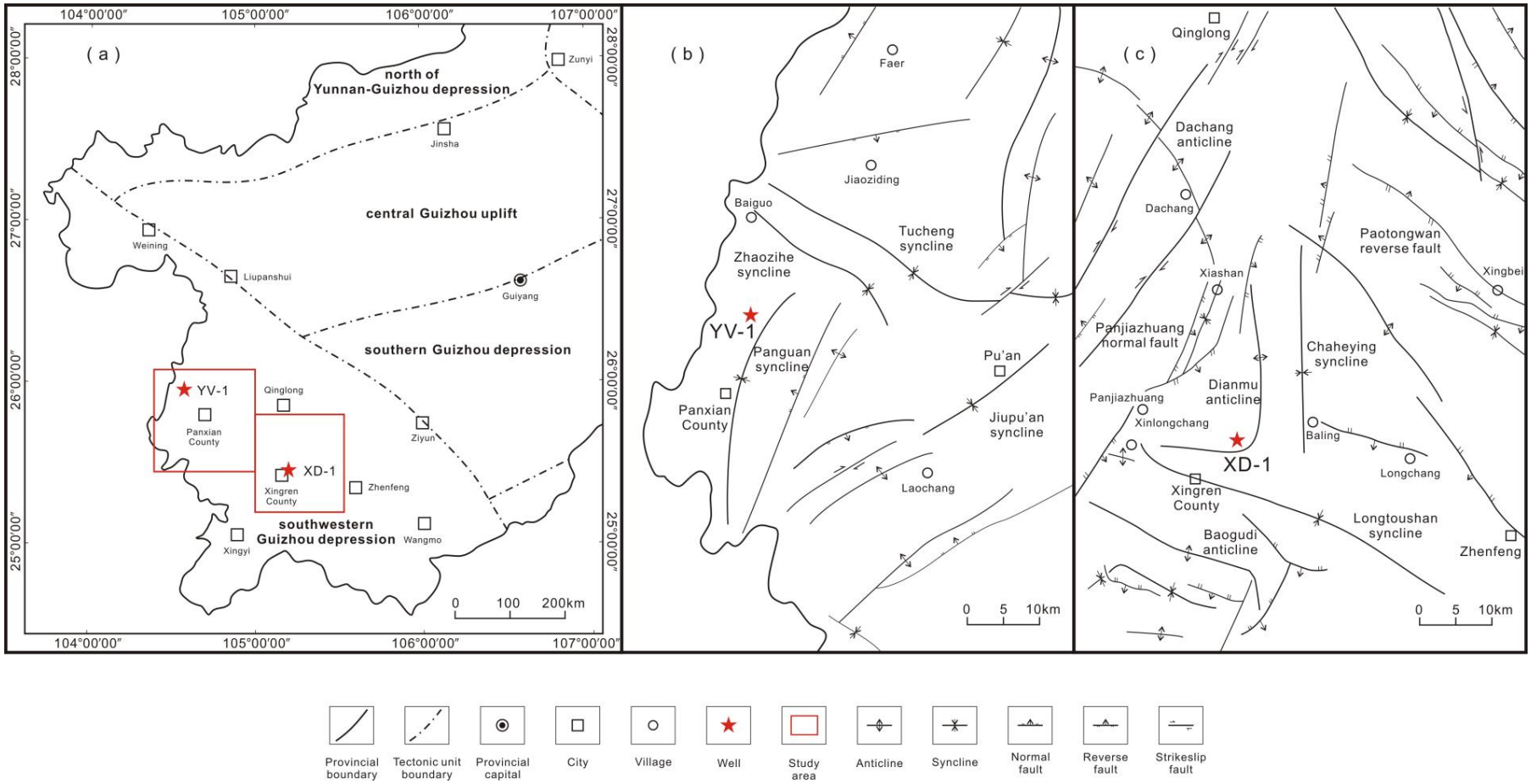

Figure 1. (**a**) Location of the study area in southwest Guizhou Province, China; (**b**) main structures in Panxian County; (**c**) main structures in Xingren County.

From the Carboniferous to Permian periods, continuous regression with multiple small-scale transgressions occurred in the southwestern of Guizhou Province. During the Late Carboniferous, the relative sea level started to rise gradually and then reached the maximum flooding surface, which marked the maximum transgression, forming a barrier coast and carbonate platform sedimentary system. In the Early Permian, the crust was uplifted by the southward subduction of the Siberia plate and the relative sea level began to fall, forming a river and delta sedimentary system. The sedimentary environment changed from epicontinental sea to lagoon, swamp and delta due to the seawater retreat in the NE direction [26,29]. In the Late Permian, the transitional Longtan Formation was deposited in an oxic depositional environment with a large amount of terrigenous input. The Kangdian Upland played an important role in organic matter accumulation [30]. The middle section of the Longtan Formation developed a thick organic-rich shale layer and was considered to have good exploration potential.

The sedimentary environment of the Late Permian varies greatly from lower delta plains, through lagoon-tidal flats, to carbonate subtidal flats in southwestern Guizhou (Figure 2a) [31]. The Longtan Formation in Panxian County represents a transitional facies dominated by delta and lower delta plains environments. It was deposited onto the Mount Emei Basalt Formation and covered by the Changxing Formation. The turbulent depositional environment caused dark mudstones frequently interbedded with silty mudstone, carbonaceous mudstone and coal seam, showing a more complex lithological assemblage in a vertical direction (Figure 2b). The thickness of Longtan Formation ranges from 170–300 m, and the thickness of organic-rich mudstone can reach 40–60 m. The Longtan Formation in Xingren County represents a transitional facies dominated by lagoon-tidal flat environments. It was also deposited between the Mount Emei Basalt Formation and the Changxing Formation. The whole suite of coal-bearing series is dominated by fine-grained sediments, which mainly consist of thin-bedded grey silty mudstone, carbonaceous shale, siliceous shale and coal seam (Figure 2c). The thickness of Longtan Formation ranges from 260–380 m, and the thickness of organic-rich shale can reach 40–100 m.

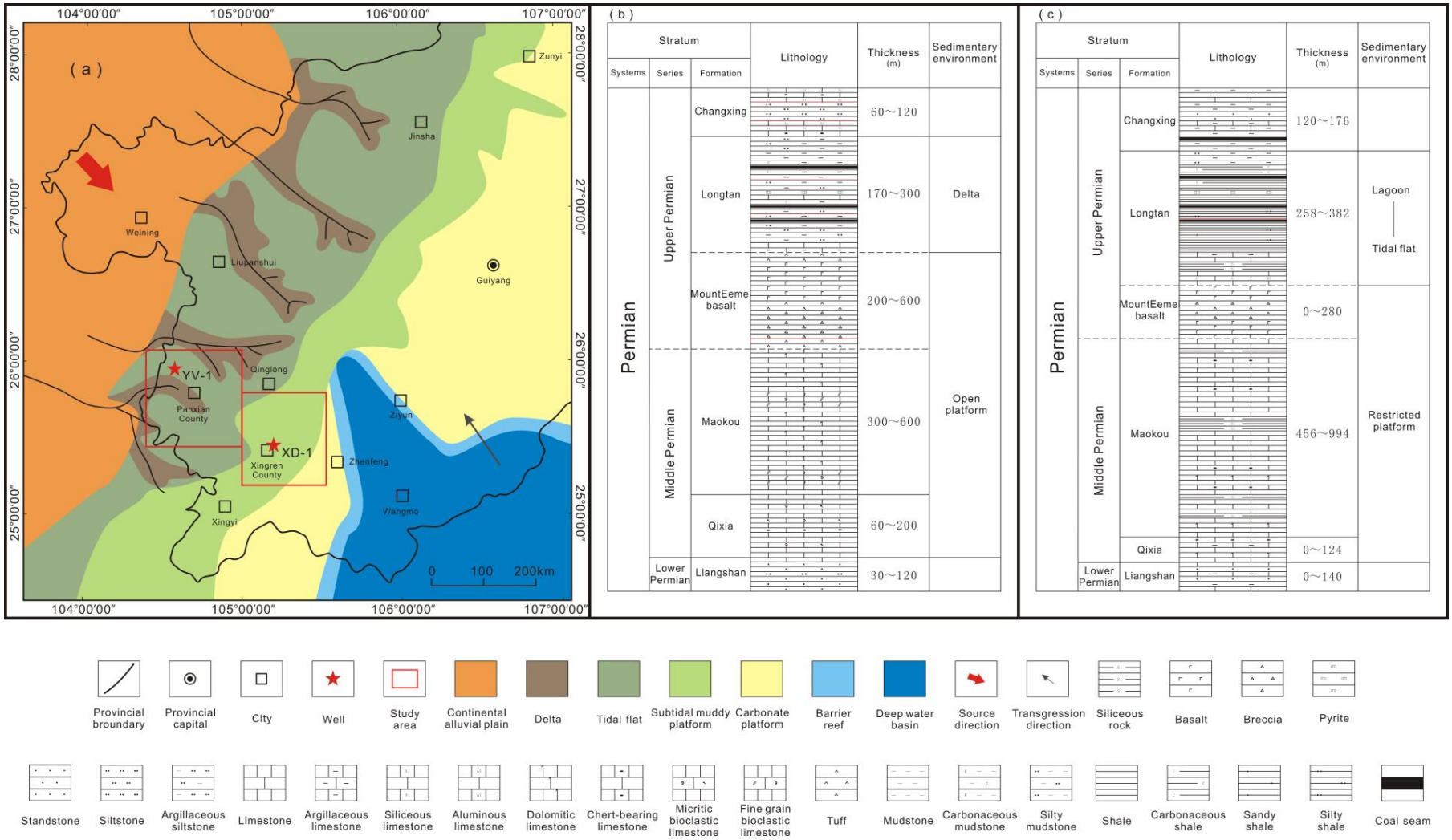

Figure 2. (**a**) Sedimentary facies in southwest Guizhou Province, modified from Dou et al. [29]; (**b**) stratigraphy in Panxian County; (**c**) stratigraphy in Xingren County.

3. Samples and Experimental Methods

A total of 18 Longtan shale samples were collected from wells in the two study areas (Figure 2a). Each sample was immediately stored in a clean plastic bag to ensure as little contamination and oxidation as possible, and then delivered to the laboratory for experiments. All samples were evaluated based on organic petrography analysis, X-ray diffraction test, methane adsorption test, mercury intrusion capillary pressure, nitrogen adsorption, carbon dioxide gas adsorption, and nuclear magnetic resonance test. The field emission scanning electron microscopy was used to observe pore geometry, and the fractal dimension was calculated to investigate the heterogeneity of the pore system.

Organic petrography analysis includes the vitrinite reflectance test, total organic carbon content test and kerogen type test. The vitrinite reflectance was determined by a Leitz MPV-SP photometer microscope (Stuttgart, Germay), following conventional methods according to the China National Standards (GB/T6948-1998). The temperature of the experiment was 22 °C and the humidity was 30%–32%. The total organic carbon content was determined by a Leco CS-200 carbon-sulfur analyzer (San Jose, MI, USA), following conventional methods according to the Chinese National Standards (GB/T19145-2003). Samples, each weighing about 1 g, were crushed to a powder at 100–200 mesh sizing and treated with 5% hydrochloric acid for 2 h to remove carbonates. The samples were then cleaned using distilled water. Afterwards, the samples were dried at 70°C for 12 h before measuring TOC content. The temperature of the experiment was 27 °C. The kerogen type was determined by a FM-252 gas isotope mass spectrometer, following carbon and oxygen isotopic analysis of organic and carbonate rocks according to the Oil and Gas Industry Standards (SY/T5238-2008). Fragments of rock were leached in 5% hydrochloric acid for 12 h to remove carbonates, then washed several times with distilled water and treated with hydrofluoric acid for 12 h to remove silicates. The relative PDB value was used to divide the kerogen type.

The XRD mineral content analysis was performed using a D8 Discover X-ray diffractometer (Bruker, Karlsruhe, Germany), following the Oil and Gas Industry Standards (SY/T5463-2010). Shale samples were crushed to less than 300 mesh sizing and mixed with ethanol, grinded a mortar, and then smear-mounted on glass slides for XRD analysis. The X-ray diffractometer with a Cu X-ray tube was operated at 40 kV and 30 mA scanning from 2° to 70° at a step of 0.02° and the data was semi-quantified by Jade® 6.0 software (Jade Software, Christchurch, New Zealand). Methane adsorption was conducted using a high-pressure gas sorption-desorption instrument from a high pressure volume analyer (HPVA) Isotherm Measurement System, following the Chinese National Standards (GB/T19560-2008). The Langmuir volume was obtained by using the Langmuir models. Samples, weighing 100–150 g, were crushed to 60–80 mesh sizing. The experimental procedure is described in detail by Zhang et al. [32].

An AutoPore IV9500 automatic mercury injection apparatus (Micromeritics Instrument Limited Company, Shanghai, China) was used to measure macropore structure (pore diameter of 50–10,000 nm). Following methods of Bustin et al. [33], samples, weighing 1–2 g, with the diameter of 3-10 mm were oven dried at 110 °C for 24 h to remove free and adsorptive water. Samples were then placed under vacuum for injection. The maximum working pressure was 413 MPa, with mercury volume precision of 0.1 μL. The pore size measurement range was 0.003–1000 μm. The Washburn equation was used to obtain the specific surface area and the pore size distribution [34].

A Quadrasorb SI surface area and porosity analyzer (Quantachrome Company, Boynton Beach, FL, USA) was used to measure mesopore structure (pore diameter of 2–50 nm). Following methods of Yang et al. [10], samples, weighing 1–2 g, were crushed to about 60–80 mesh size and vacuum treated for 3 h at 300 °C to eliminate residual and capillary water. Nitrogen adsorption at different relative pressure was measured at 77.35 K, with high purity nitrogen as medium. The pore size measurement range was 0.35–400 nm and the relative pressure range of adsorption-desorption was 0.004 to 0.995. The Brunauer–Emmett–Teller (BET) model was applied to obtain the SSA, and the Barrette–Joynere–Halenda (BJH) model was used for PV and PSD [35].

A NOVA4200e surface area and porosity distribution analyzer (Quantachrome Company, Boynton Beach, FL, USA) was used to measure micropore structure (pore diameter of 0–2 nm). Micropore structure can be characterized by measuring isothermal adsorption of CO_2 at 0 °C, for CO_2 can enter pores having a diameter less than 0.36 nm. Following methods of Liu and Wilcox [36], samples, weighing 1–2 g, were crushed to about 100 mesh and then subjected to degassing under vacuum for 20 h at 110 °C. The pore size measurement range was 0.35–2 nm. The Dubinin–Astakhov (D–A), Dubinin–Radushkevich (D–R) and Density Function Theory (DFT) models were used for PV, SSA and PSD, respectively [37].

NMR measurement was performed by a RecCore-04 NMR analyzer (Renheng Commercial and Trading Limited Company, Langfang, China), following the Oil and Gas Industry Standards (SY/T6490-2000), with the same experimental procedure as shown in previous research [13]. Samples were dried for 24 h in a dry box at 70 °C, vacuumed for 8 h and then saturated for 8 h in distilled water to complete the pretreatment. The NMR parameters were installed by echo spacing (T_E) of 0.6 ms, waiting time (T_W) of 5000 ms, maximum echo numbers (N_E) of 1024, and scanning numbers (SCAN) of 128. Porosity and permeability was measured by NMR test.

A Quanta 200F scanning electron microscope (FEI Company, Hillsborough, OR, USA) was used for imaging. Sample with 1 cm^3 piece was polished by a TechnoorgSC-100 argon-ion cross-section polisher (Nanjing Tansi Science and Technology Limited Company, Nanjing, China) to remove impurities, creating a pristine 2-D surface. After polishing, the thin sections were attached to sample table with conductive adhesive, and polishing surface was coated with a 10 nm gold film to enhance its conductivity [27]. The back-scattering electron mode was chosen to observe the different cross sections of each sample at a temperature of 24 °C and a humidity level of 35%.

The FHH model is widely used and has been shown to be the most effective method for describing the irregular geometric and structural properties of shale. The log–log terms equation to calculate the nitrogen adsorption fractal dimension using the FHH model is [12]: $\ln(V) = C + (D - 3) \times \ln(\ln(P_0/P))$, where V ($cm^3/g$) is the volume of adsorbed nitrogen at an equilibrium pressure P, P_0 (MPa) is the gas saturation pressure, C is a characteristic constant and D is the fractal dimension. The ln(V) and $\ln(\ln(P_0/P))$ are linearly correlated in shales with fractal characteristics. With this equation, we can obtain the slope of ln(V) vs. $\ln(\ln(P_0/P))$ by regression analysis to calculate the nitrogen adsorption fractal dimension D.

4. Results

4.1. Organic Geochemical Characteristic

4.1.1. Total Organic Matter Content

Both YV-1 and XD-1 shale samples possess high TOC contents (Table 2), indicating that shales investigated are rich in organic matter. The TOC content of YV-1 is between 2.36% and 6.40%, with an average value of 4.82%, and the TOC content of XD-1 is between 0.89% and 6.85%, with an average value of 4.38%. The TOC content of YV-1 is relatively higher than that of XD-1, which may be related to the enrichment of coals in Panxian County. Shales that inbedded with coal seams can show extremely high TOC values [37–40]. Higher TOC implies higher gas generation potential and better adsorption capacity. The lower limit of TOC for commercial exploitation of shale gas is generally 2.0% [41]. However, approximately 88.8% of the TOC values in the study area exceed 2%, and the accumulative shale thickness with TOC > 2% is greater than 60 m, indicating that most samples could have good shale gas resource potential.

Table 2. Organic geochemical test results of transitional Longtan Shale samples from YV-1 and XD-1.

Sample	Depth (m)	TOC (wt.%)	R_o (%)	δ^{13} C (‰)	Kerogen Type *
Y-1	358.5	5.38	0.86	−24.9	III
Y-2	587.0	2.36	1.03	−23.6	III
Y-3	678.0	6.40	1.15	−24.8	III
Y-4	828.6	4.68	1.17	−23.8	III
Y-5	852.6	4.92	1.06	−23.4	III
Y-6	928.8	5.18	1.02	−24.4	III
X-1	1075.5	0.89	2.50	−24.3	III
X-2	1103.0	6.85		−24.6	III
X-3	1175.8	1.99		−24.3	III
X-4	1219.6	4.87	2.56	−24.5	III
X-5	1234.3	3.60		−24.2	III
X-6	1286.3	3.30		−24.5	III
X-7	1328.6	5.23	2.76	−23.2	III
X-8	1339.5	4.21		−23.4	III
X-9	1355.1	5.27		−24.6	III
X-10	1365.5	5.23		−24.2	III
X-11	1376.2	4.34		−24.4	III
X-12	1443.8	6.80	2.93	−23.5	III

* Type-I with δ^{13} C less than −28‰, type-II_1 with δ^{13} C of −28‰–26.5‰, type-II_2 with δ^{13} C of −26.5‰–25‰, and type-III with δ^{13} C more than −25‰.

4.1.2. Thermal Maturity

The vitrinite reflectance (% R_o) value is used to evaluate the maturation level. Geochemical test results in Table 2 demonstrate that the YV-1 samples have low R_o values, varying from 0.86% ± 0.070% to 1.17% ± 0.068%. The XD-1 samples are higher than the YV-1 shales in R_o values, varying from 2.50% ± 0.149% to 2.93% ± 0.193%. It suggests that the YV-1 samples are low matured and thermal maturity has been in the oil window, while the XD-1 samples are over matured and thermal maturity has been in the dry-gas window.

4.1.3. Organic Matter Type

Different organic matter (OM) types, which can affect the hydrocarbon generation type [42], are derived from different primary production. The compositional characteristics of kerogen can reveal the changes in the depositional environment during sedimentation [43]. All samples in this study had stable carbon isotope ($^{13}\delta C_{PDB}$) values from −24.9‰ to −23.2‰ (Table 2), indicating the organic matter is gas-prone type III kerogen dominated by vitrinite group macerals and to a lesser extent inertinite group macerals (Figure 3). The result is consistent with the characteristic of depositional environment of the transitional Longtan Shale. The accumulation of OM mainly relies on a large amount of terrigenous input from the Kangdian Upland.

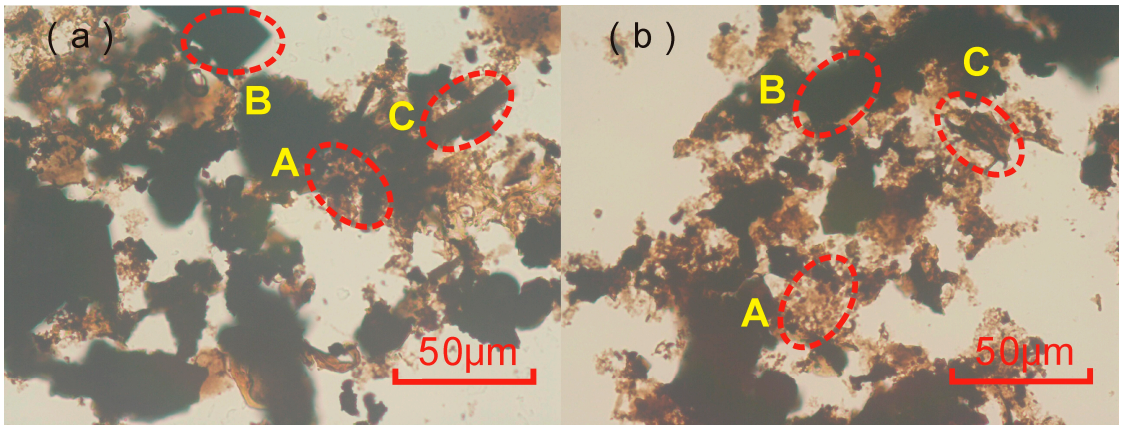

Figure 3. Macerals of transitional Longtan Shale samples from YV-1 (**a**) and XD-1 (**b**). A is brown dispersed sapropelic component; B is black inertinite; C is brown strip vitrinite.

4.2. Mineralogical Composition

The mineral composition primarily reflects the depositional environments and diagenetic evolution of the shales during their sedimentation and maturation [10]. The mineral compositions include clay minerals, brittle minerals (including quartz, plagioclase and pyrite) and carbonate minerals (including calcite, dolomite and siderite). The result, presented in Table 3, shows that the mineral composition of shales in the two study areas is significantly different. The YV-1 samples are dominated by clay minerals (71.33% average), followed by brittle minerals (27.50% average). The proportion of clay minerals, brittle minerals and carbonate minerals in XD-1 is similar (on average 37%, 30.25% and 32.75%, respectively). The ternary diagram (Figure 4) shows that, compared with XD-1, the YV-1 is rich in clay minerals but poor in carbonate minerals. These differences may be related to the depositional environments and further affect the pore characteristics and adsorption capacity of shale [44,45]. Shales deposited in the deep-water marine shelf are usually characterized by a high content of siliceous minerals and low contents of clay minerals. Previous studies have shown that clays, with larger surface area, have a positive relationship with gas sorption capacity [46]. However, unlike brittle mineral-rich shale, clay mineral-rich shale is not conducive to the formation of fractures. Thus, the extremely high clay content may be a problem for shale gas development in Panxian County.

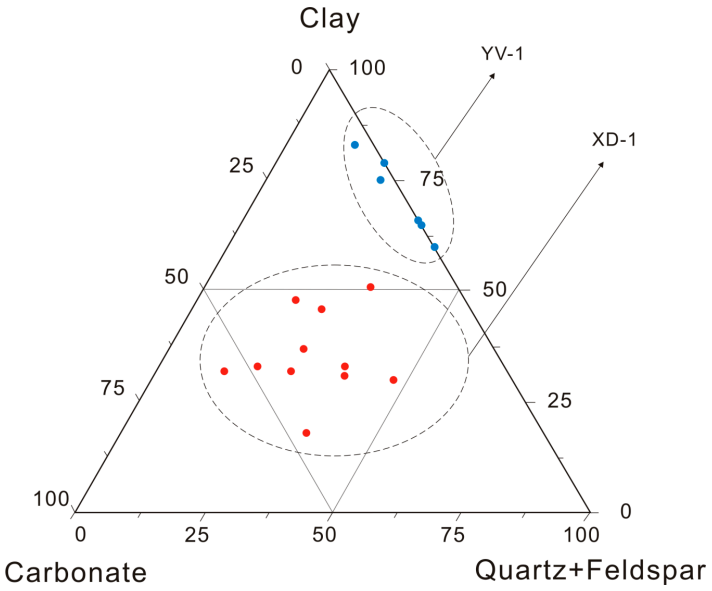

Figure 4. Mineralogical ternary diagram of transitional Longtan Shale samples from YV-1 and XD-1.

Analyses (Figure 5) show that the predominant clay mineral of YV-1 samples is the mixed-layer of illite and smectite (I/S), followed by chlorite and kaolinite (on average 41.67%, 29.33% and 26%, respectively). In XD-1, the clays are mainly represented by I/S (61.33% average) and illite (28.83% average), with a very small proportion of chlorite and kaolinite. Guo et al. [47] indicated that the assemblage pattern of clays can reflect the diagenetic level of the source rock to some extent. The variation mainly presents the transformation process of the clay minerals from kaolinite to illite and I/S during continuous compaction in the middle diagenetic stage. The XD-1 shales, with a larger amount of I/S, are in a higher diagenesis level than the YV-1 shales, which is consistent with the maturity test result.

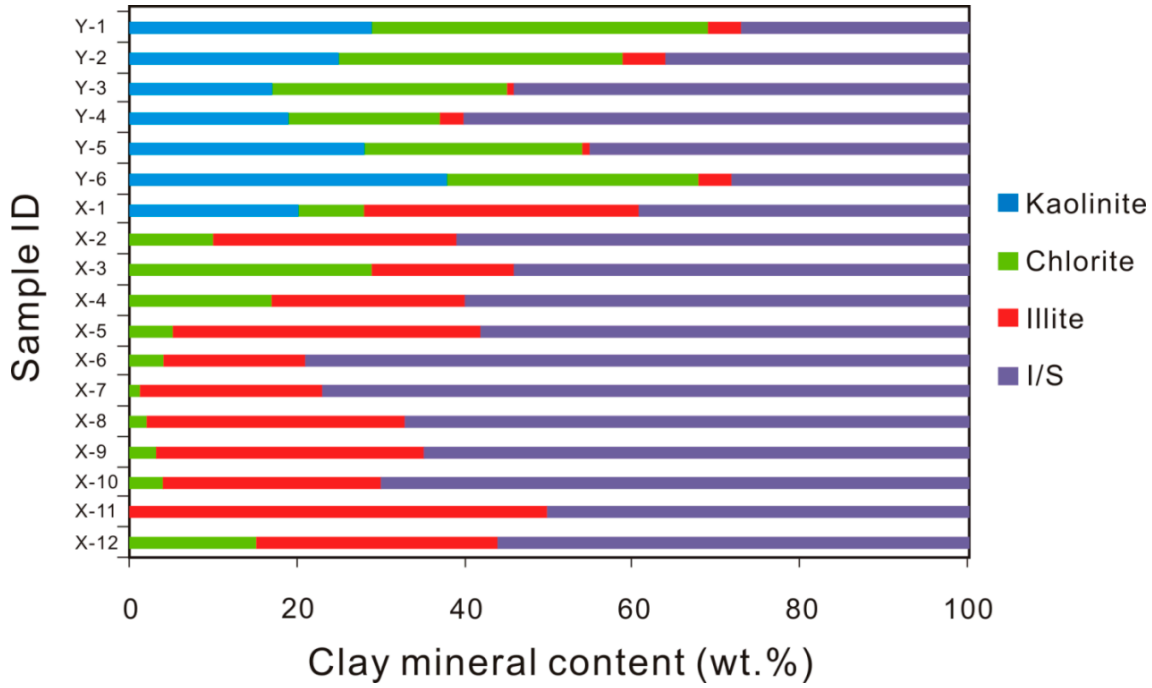

Figure 5. Clay mineral composition of transitional Longtan Shale samples from YV-1 and XD-1.

The relationships between TOC content and clay mineral content of YV-1 and XD-1 are illustrated in Figure 6a, suggesting that there is a positive correlation between TOC and clays (R^2 = 0.682 and 0.587, respectively). Most organic matter in argillaceous source rocks is distributed in clay minerals as dispersed or locally enriched. However, transitional shales in this study have complex lithological changes and mineral composition, and organic matter is also filled in pores of other minerals, which leads to the moderate correlations between TOC and clay minerals. As shown in Figure 6b, samples of YV-1 show a significant negative correlation between TOC content and quartz content (R^2 = 0.949), while samples of XD-1 show no obvious correlation between TOC and quartz. The conclusion is different with some previous studies, which suggested a positive relationship between TOC and quartz content [27]. However, these differences may be related to the depositional environments. Quartz was thought to be positively correlated with TOC if the shale was biogenic in origin and negatively correlated with TOC if the origin was detrital [19]. The Longtan Formation Shale was mainly deposited in a delta and lagoon-tidal flat system, and the Kangdian Upland is the dominant sediment source region. The SEM image in Figure 13h also shows a smooth quartz surface with no pores. Thus, the most of quartz in this study did not have a biogenic origin.

Table 3. Mineralogy composition of transitional Longtan Shale samples from YV-1 and XD-1.

Sample	Clay (wt.%)	Quartz (wt.%)	Feldspar (wt.%)	Calcite (wt.%)	Dolomite (wt.%)	Pyrite (wt.%)	Siderite (wt.%)	Kaolinite (wt.%)	Cholorite (wt.%)	Iillite (wt.%)	I/S * (wt.%)
Y-1	79	17	0	0	0	4	0	29	40	4	27
Y-2	60	32	0	0	0	8	0	25	34	5	36
Y-3	83	13	0	2	0	0	2	17	28	1	54
Y-4	65	19	7	0	0	9	0	19	18	3	60
Y-5	75	20	2	1	0	0	2	28	26	1	45
Y-6	66	15	0	0	0	19	0	38	30	4	28
X-1	18	30	0	16	28	6	2	20	8	33	39
X-2	53	22	8	0	0	17	0	0	10	29	61
X-3	33	25	8	0	27	3	4	0	29	17	54
X-4	32	15	9	0	29	2	13	0	17	23	60
X-5	30	33	8	0	23	6	0	0	5	37	58
X-6	32	6	4	0	43	3	12	0	4	17	79
X-7	51	17	11	0	13	4	4	0	1	22	77
X-8	33	15	4	0	48	0	0	0	2	31	67
X-9	46	11	8	0	27	6	2	0	3	32	65
X-10	48	10	7	0	23	2	10	0	4	26	70
X-11	31	19	8	9	23	10	0	0	0	50	50
X-12	37	20	2	0	37	4	0	0	15	29	56

* I/S is the mixed-layer of illite and smectite.

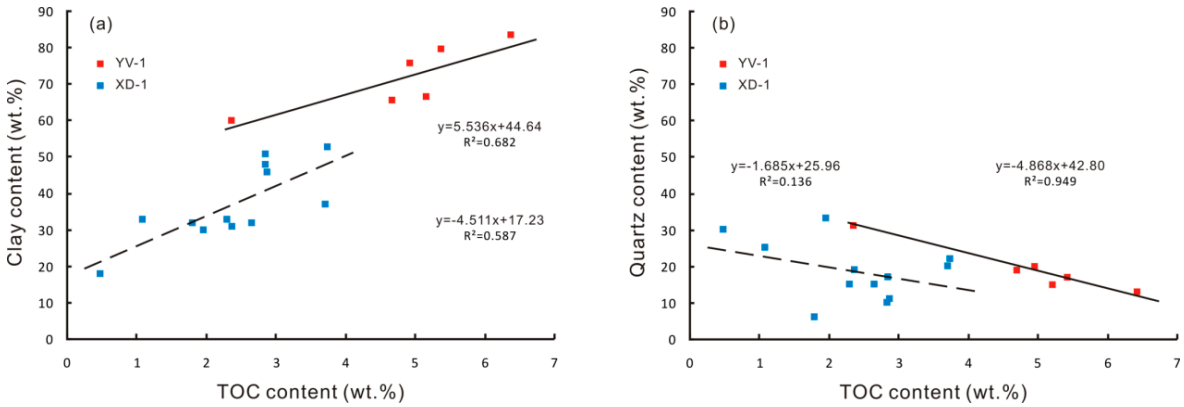

Figure 6. Relationships between TOC content and clay content (**a**), quartz content (**b**) of transitional Longtan Shale samples from YV-1 and XD-1.

4.3. Porosity, Permeability, and Methane Adsorption Results

Porosity and permeability are important parameters to reflect the storage capacity. The porosity of the YV-1 ranges from 0.91% to 2.44% with an average value of 1.69%, and the permeability ranges from 0.20 $\times$ 10^{-5} mD to 1.25 $\times$ 10^{-5} mD with an average value of 0.49 $\times$ 10^{-5} mD. The porosity of the XD-1 varies between 0.87% and 3.42% with an average value of 1.82%, and the permeability varies between 0.003 $\times$ 10^{-5} mD to 1.917 $\times$ 10^{-5} mD with an average value of 0.28 $\times$ 10^{-5} mD (Table 4). The permeability of YV-1 samples is significantly lower than that of XD-1. Nie et al. [48] suggested that lower limits of porosity and permeability for shale gas reservoir is 1% and 0.001 mD, respectively. The results showed that the permeability of shale in this study is quite low.

Table 4. Porosity, permeability and methane adsorption capacity of transitional Longtan Shale samples from YV-1 and XD-1.

Sample	Porosity (%)	Permeability (10^{-5} mD)	Langmuir Volume (m^3/t)
Y-1	1.78	0.432	2.23
Y-2	2.44	1.246	2.14
Y-3	1.94	0.362	3.78
Y-4	1.65	0.340	2.02
Y-5	1.46	0.363	3.34
Y-6	0.91	0.200	2.30
X-1	1.86	0.020	2.34
X-2	2.82	0.068	3.41
X-3	1.11	0.005	2.54
X-4	1.39	0.005	2.84
X-5	1.74	0.008	2.82
X-6	1.02	0.003	2.77
X-7	1.61	1.917	3.11
X-8	1.76	0.206	2.93
X-9	2.61	1.099	3.12
X-10	3.42	0.055	3.21
X-11	1.58	0.010	3.04
X-12	0.87	0.003	3.39

The amount of adsorbed methane gas may be affected by adsorption capacity and pore structure characteristic, which could have a significant impact on shale gas exploration. As shown in Table 4, the Langmuir volume (V_L) of the YV-1 samples ranges from 2.02 m^3/t to 3.78 m^3/t, with an average value of 2.64 m^3/t, while the Langmuir volume (V_L) of the XD-1 samples ranges from 2.34 m^3/t to 3.41 m^3/t, with an average value of 2.96 m^3/t. Samples of XD-1 have higher methane adsorption capacity than YV-1.

4.4. Pore Structure Qualitative and Quantitative Characterization between Shales with Different Sedimentary Microfacies

4.4.1. Pore Structure Qualitative Characterization through N_2 Adsorption–Desorption Isotherms

The heterogeneity throughout the shale makes the pore characteristics differ remarkably from sample to sample. The typical isotherms for the low-pressure N_2 adsorption–desorption analysis of the two different sedimentary facies shales are illustrated in Figure 7. The adsorption isotherms of samples are slightly different in shape, but all in the form of anti "S" type. According to the International Union of Pure and Applied Chemistry (IUPAC) classification [2], most of them belong to type IV curves [49,50], while some of the samples in XD-1 are characterized by the both features of the type IV and type I. The isotherm curves of the YV-1 show a maximum adsorbed volume at intermediate relative pressure interval ($0.2 < P/P_0 < 0.95$), but extremely low adsorbed volume at high relative pressure interval ($P/P_0 > 0.95$), indicating the large existence of the small pores and no significant amount of large pores. The isotherm curves of the XD-1 show relatively low adsorbed volume from low to intermediate relative pressure interval ($P/P_0 < 0.2$ and $0.2 < P/P_0 < 0.95$), but a maximum adsorbed volume at high relative pressure interval ($P/P_0 > 0.95$), suggesting that samples lack small pores but have a large amount of large pores.

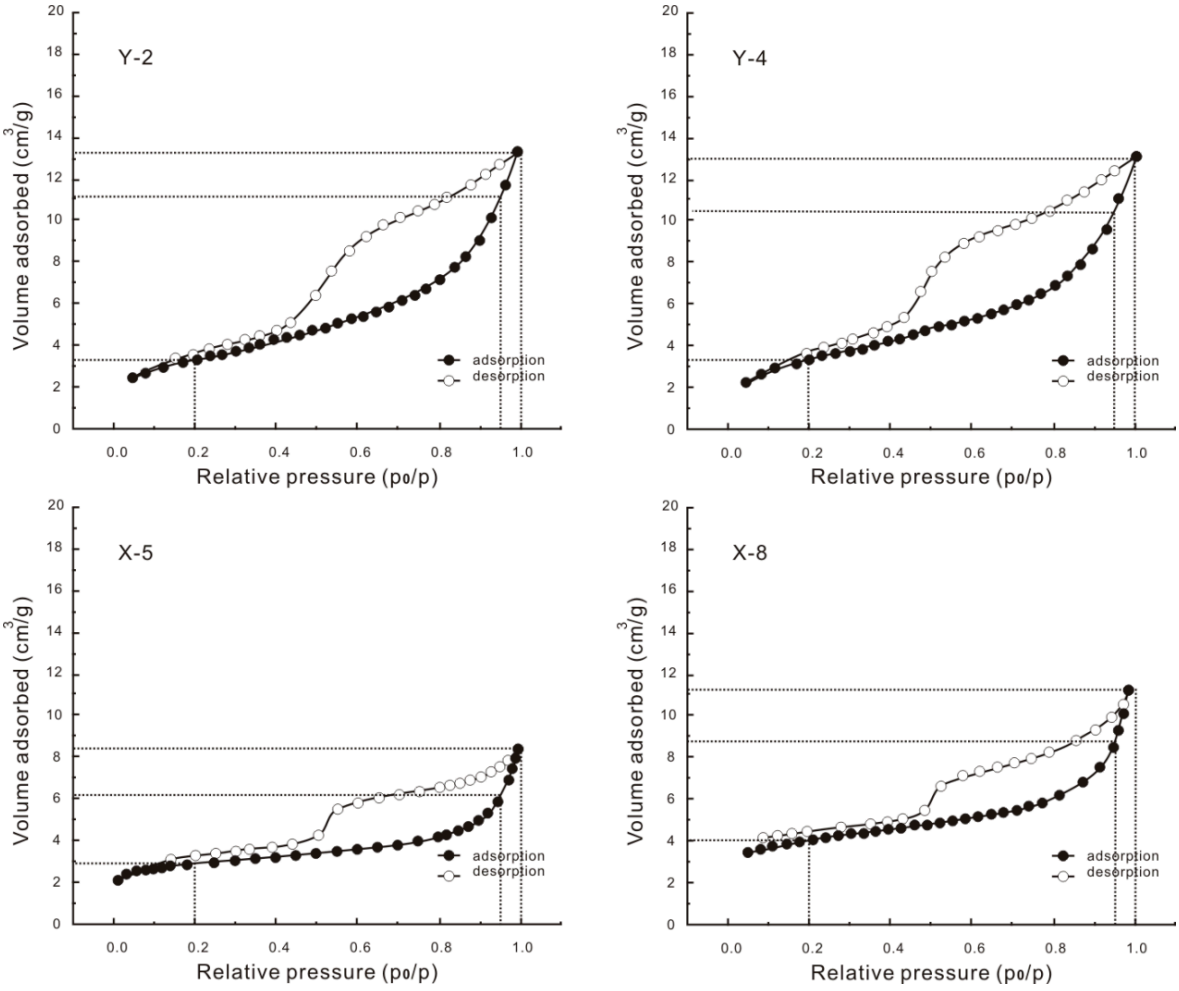

Figure 7. Typical N_2 adsorption-desorption isotherms of transitional Longtan Shale samples from YV-1 and XD-1.

The adsorption branch of isotherms is inconsistent with the desorption branch at higher relative pressures ($P/P_0 > 0.5$), resulting in a hysteresis loop. Using the type of the hysteresis

loops to predict pore shape [51], samples of XD-1 can be divided into type H_2 hysteresis, which indicates ink bottle-shaped pores. Samples of YV-1 can be mainly classified as H_3 type hysteresis, which indicates slit-shaped pores and wedge-shaped pores. The shape of hysteresis loops of some samples is somewhere between type H_3 and H_2, which may be related to a combination of different pore types. The previous studies [52,53] suggested that ink bottle-shaped pores (type H_2) can be considered as the OM-hosted pores, while wedge-shaped pores (type H_3) can be considered as the clay mineral-hosted pores.

4.4.2. Pore Structure Qualitative Characterization through Nuclear Magnetic Resonance T_2 spectrum

The nuclear magnetic resonance (NMR) T_2 spectrum in this study can be divided into unimodal spectrum and bimodal spectrum (Figure 8). The unimodal spectra are frequently found in samples of XD-1 with a relatively short relaxation time (T_2 = 2 ms), indicating that small pores occupy a large proportion of the signal and are well developed. The bimodal spectra are frequently found in samples of YV-1, suggesting that besides small pores, large pores are also developed. Take sample Y-6 as an example, we observed two peaks before centrifuge processing, and the first peak was much higher than the second one. The discontinuity of bimodal spectrum indicates that samples have poor connectivity between small pores and large pores, and the pores in samples are relatively closed. After centrifuge processing, the first peak attenuated and the second peak vanished. The reduction and disappearance were due to the connectivity between pores, which was a result of the different permeability [27].

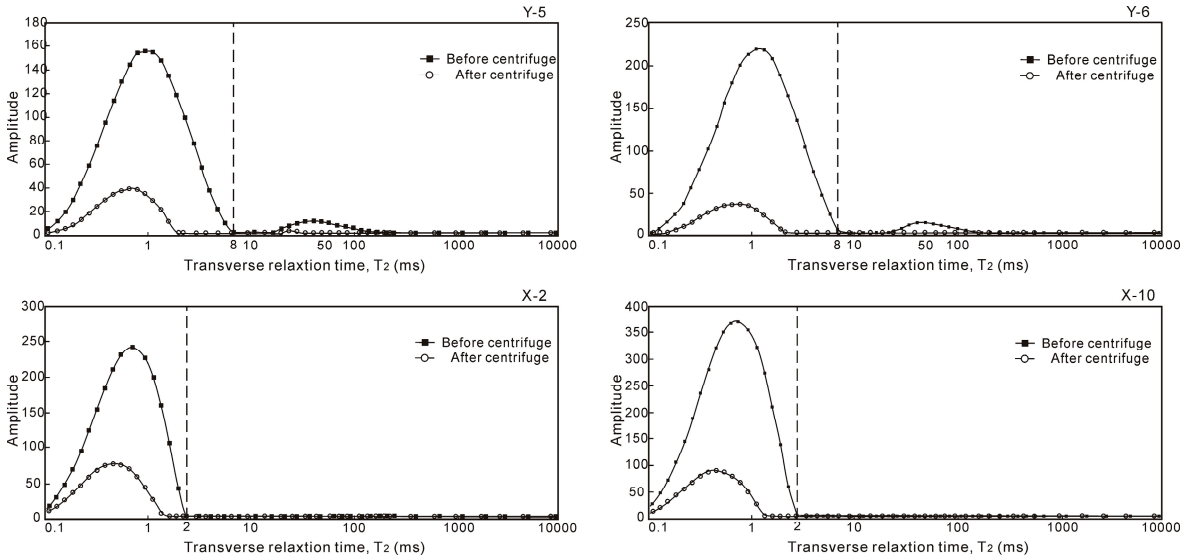

Figure 8. Typical nuclear magnetic resonance (NMR) T_2 spectra of transitional Longtan Shale samples from YV-1 and XD-1.

4.4.3. Pore Structure Qualitative Characterization through Fractal Dimension

The fractal dimension (D) can reflect the pore surface roughness and the pore structure complexity. According to N_2 adsorption-desorption data and fractal FHH model, the fractal dimension of shale samples can be calculated by the slope of ln(V) vs. ln(ln(p/p_0)). As shown in Figure 9, the ln(V) vs. ln(ln(p/p_0)) is linearly correlated, with good fitting correlation coefficients. The results in Table 5 show that different samples have different fractal characteristics. The fractal dimension of YV-1 is in the range of 2.652–2.862, with an average value of 2.756, while the fractal dimension of XD-1 is in the range of 2.702–2.867, with an average value of 2.787. The fractal dimension of XD-1 is slightly higher than that of YV-1, indicating a more rough pore surface and a more complicated pore structure.

Table 5. Fractal dimension of transitional Longtan Shale samples from YV-1 and XD-1.

Sample	Fitting Equation	Fitting Cofficent (R^2)	Fractal Dimension
Y-1	y = −0.201x + 2.361	0.857	2.799
Y-2	y = −0.263x + 1.444	0.891	2.737
Y-3	y = −0.138x + 1.912	0.840	2.862
Y-4	y = −0.348x + 1.457	0.980	2.652
Y-5	y = −0.187x + 1.514	0.873	2.813
Y-6	y = −0.328x + 1.408	0.965	2.672
X-1	y = −0.298x + 0.967	0.998	2.702
X-2	y = −0.186x + 1.122	0.992	2.814
X-3	y = −0.204x + 1.061	0.976	2.796
X-4	y = −0.245x + 1.011	0.995	2.755
X-5	y = −0.209x + 0.247	0.988	2.791
X-6	y = −0.211x + 1.696	0.997	2.789
X-7	y = −0.186x + 1.265	0.994	2.814
X-8	y = −0.222x + 1.029	0.980	2.778
X-9	y = −0.208x + 1.133	0.995	2.792
X-10	y = −0.217x + 1.490	0.997	2.783
X-11	y = −0.233x + 0.863	0.994	2.767
X-12	y = −0.133x + 1.527	0.993	2.867

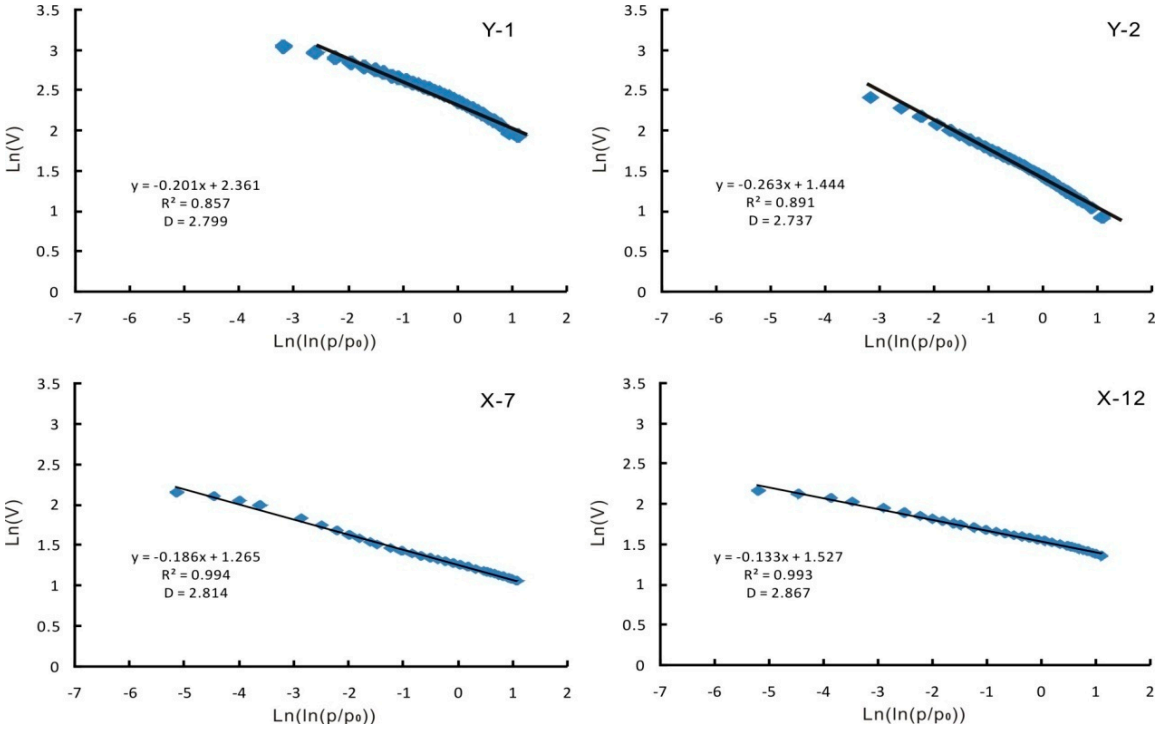

Figure 9. Typical polts of ln(V) vs. $\ln(\ln(p/p_0))$ of transitional Longtan Shale samples from YV-1 and XD-1.

4.4.4. Pore Structure Quantitative Characterization through Mercury Intrusion Capillary Pressure (MICP) and Gas Adsorption

Pores has been divided into micropore (pore diameter < 2.0 nm), mesopore (pore diameter of 2.0–50 nm) and macropore (pore diameter > 50 nm) by IUPAC. Micropore structure was quantified by CO_2 adsorption, and the PV, SSA and PSD were obtained by the D–A, D–R and DFT models, respectively. Mesopore structure was quantified by N_2 adsorption, and the PV, SSV and PSD were obtained by the BJH, BET and BJH models, respectively. Macropore structure was quantified by MICP, and the PV, SSA and PSD were obtained by cumulative mercury volume, the Young–Dupré equation,

and the Washburn equation, respectively [34,35,37,54]. The superimposed parts were handled using mathematical and statistical methods, and the average diameter of shale pore was calculated based on the following equation [55]: $(4V_p/A_s) \times 2$, where V_p = total pore volume of the shale, and A_s = total specific surface area of the shale.

The PV, SSA and average pore diameter of YV-1 and XD-1 shale samples are shown in Table 6. The PV of YV-1 varies from 0.01948 cm^3/g to 0.03556 cm^3/g, with a mean value of 0.02881 cm^3/g. The SSA varies from 15.161 m^2/g to 26.315 m^2/g, with a mean value of 20.806 m^2/g. The average pore diameter ranges from 9.99 nm to 11.95 nm, with a mean value of 11.07 nm. While, the PV of XD-1 varies from 0.01021 cm^3/g to 0.03043 cm^3/g, with a mean value of 0.02110 cm^3/g. The SSA varies from 10.668 m^2/g to 28.021 m^2/g, with a mean value of 20.101 m^2/g. The average pore diameter ranges from 6.39 nm to 13.42 nm, with a mean value of 8.40 nm. Samples of YV-1 possess larger PV, SSA and average pore diameter than XD-1 (Figure 10a,b). The relationships between PV and SSA of shale samples indicate a significant positive correlation (R^2 = 0.851 and 0.653 in Figure 11). There is no obvious correlation between average pore diameter and PV, SSA. The result different from previous studies [14,56] which suggest that PV and SSA decreased with the increase of pore diameter.

Detailed features of micropore, mesopore and macropore suggest that the pore composition of YV-1 and XD-1 have significant differences. The average micro-, meso-, and macro- PV values of YV-1 are 0.00271 cm^3/g, 0.02077 cm^3/g and 0.0053 cm^3/g, accounting for 9.41%, 72.19% and 18.40% of the total pore volume, respectively. While the average micro-, meso-, and macro- PV values of XD-1 are 0.00320 cm^3/g, 0.01136 cm^3/g and 0.0065 cm^3/g, accounting for 15.35%, 53.84% and 30.81% of the total pore volume, respectively (Table 6 and Figure 10c). Mesopore volume of the YV-1 samples is significantly larger than that of the XD-1, causing it to have a larger total pore volume than XD-1. However, micropore volume and macropore volume of YV-1 samples are slightly smaller than that of XD-1. In the YV-1 samples, mesopore occupies an absolute advantage and is the predominant contributor to PV. While, in the XD-1 samples, macropore and micropore also occupy a certain proportion in addition to mesopore (Figure 10c). The development of mesopores may originate from intraparticle pores and interparticle pores in clay minerals, and the development of micropores may be related to organic matter pores produced during hydrocarbon generation. However, considering the difference between sampling depth, lithostratigraphic pressure also has certain effects on pore composition. In XD-1, interpariticle pores occurred between clay particles are more easily deformed or closed by compaction (Figure 13g), thus reducing the proportion of mesopore.

The average micro-, meso-, and macro-SSA values of YV-1 are 8.9595 m^2/g, 11.8084 m^2/g and 0.0383 m^2/g, accounting for 41.41%, 56.75% and 1.84% of the total specific surface area, respectively, while the average micro-, meso-, and macro-SSA values of XD-1 are 10.1204 m^2/g, 9.9588 m^2/g and 0.0209 m^2/g, accounting for 50.35%, 48.61% and 1.04% of the total specific surface area, respectively (Table 6 and Figure 10d). Similar to the pore volume distribution, samples of XD-1 have larger micropore specific surface area, while samples of YV-1 have larger mesopore specific surface area because of the extremely high clay content. Micropore and mesopore are the main contributors to SSA, while the contribution of macropore is negligible (Figure 10d).

Table 6. Micropore, mesopore, and macropore structure parameters of transitional Longtan Shale samples from YV-1 and XD-1 determined by gas adsorption and MICP techniques.

Sample	CO_2 and N_2 Adsorption		MICP	CO_2 and N_2 Adsorption		MICP	Total Pore Volume (cm^3/g)	Total Surface Area (m^2/g)	Average Diameter Calc. (nm)
	D–A Micropore Volume (cm^3/g)	BJH Mesopore Volume (cm^3/g)	Macropore Volume (cm^3/g)	D–R Micropore Surface Area (m^2/g)	BET Mesopore Surface Area (m^2/g)	Calc. Macropore Surface Area (m^2/g)			
Y-1	0.00328	0.02351	0.0061	10.528	15.751	0.036	0.03289	26.315	9.99
Y-2	0.00230	0.01418	0.0030	7.603	7.544	0.014	0.01948	15.161	10.28
Y-3	0.00248	0.02688	0.0062	8.433	16.131	0.048	0.03556	24.612	11.56
Y-4	0.00277	0.01754	0.0068	9.271	8.808	0.071	0.02711	18.150	11.95
Y-5	0.00260	0.02466	0.0045	8.567	12.794	0.030	0.03176	21.391	11.88
Y-6	0.00282	0.01783	0.0054	9.355	9.822	0.031	0.02605	19.208	10.85
X-1	0.00113	0.00917	0.0076	3.402	7.258	0.008	0.01790	10.668	13.42
X-2	0.00663	0.01620	0.0076	18.279	8.448	0.007	0.03043	26.734	9.11
X-3	0.00241	0.00883	0.0061	7.861	8.770	0.014	0.01734	16.645	8.33
X-4	0.00145	0.00935	0.0099	4.674	9.448	0.002	0.02070	14.124	11.73
X-5	0.00220	0.01160	0.0029	7.29	9.542	0.025	0.01670	16.857	7.93
X-6	0.00214	0.00477	0.0033	7.156	3.952	0.011	0.01021	11.119	7.35
X-7	0.00454	0.01310	0.0050	14.645	7.996	0.077	0.02264	22.718	7.97
X-8	0.00305	0.01100	0.0048	9.816	10.846	0.014	0.01885	20.676	7.29
X-9	0.00364	0.01480	0.0039	11.919	13.665	0.049	0.02234	25.633	6.97
X-10	0.00347	0.01720	0.0090	11.174	16.823	0.024	0.02967	28.021	8.47
X-11	0.00295	0.00941	0.0068	9.625	14.343	0.01	0.01916	23.978	6.39
X-12	0.00520	0.01090	0.0112	15.604	8.426	0.01	0.02730	24.040	9.09

MICP = Mercury Intrusion Capillary Pressure; Calc. = Calculated by the Washburn Equation; D–A = Dubinin–Astakhov; BJH = Barrett–Joyner–Halenda; D–R = Dubinin–Radushkevich; BET = Barrett–Emmett–Teller; Diameter Calc. = Diameter Calculated by the Equation $(4V_p/A_s) \times 2$, where V_p = total pore volume of the shale, and A_s = total specific surface area of the shale [55].

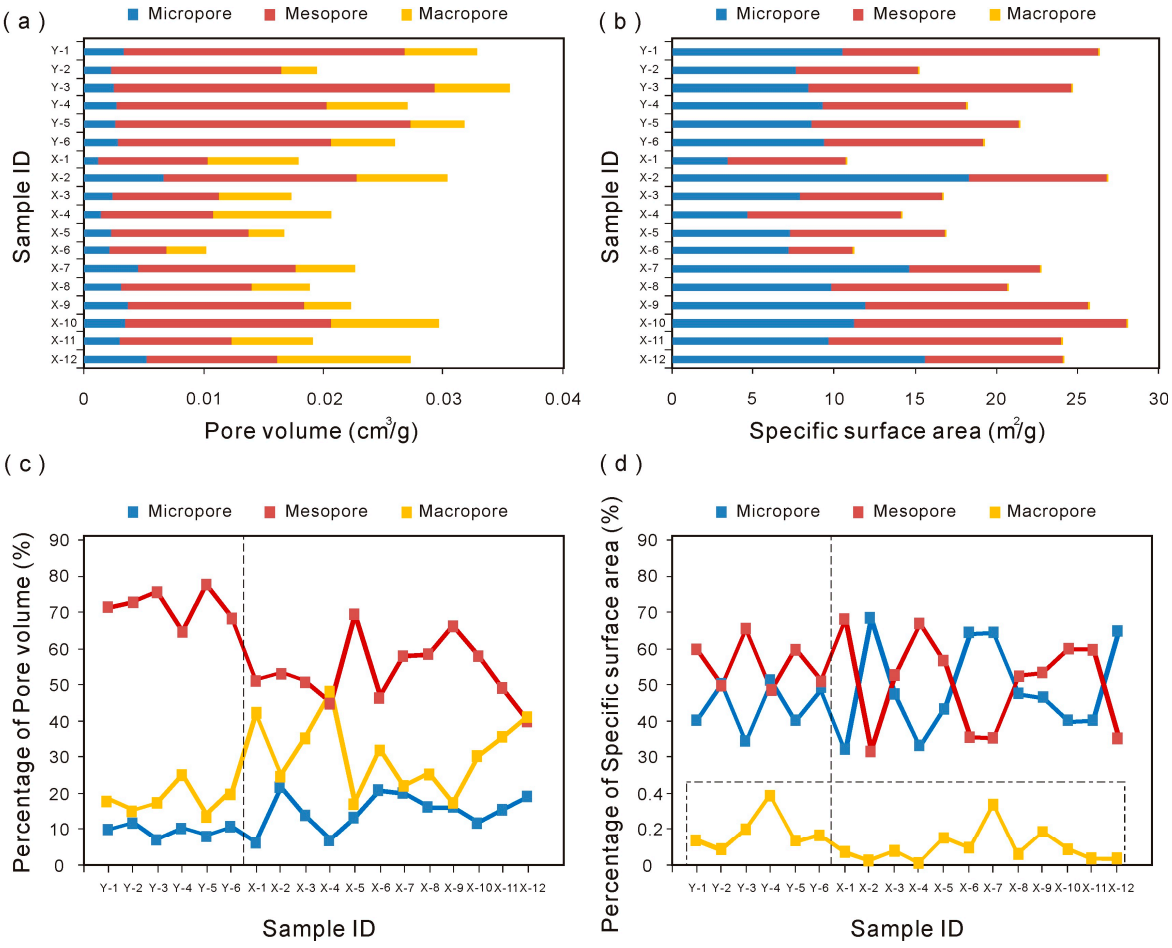

Figure 10. The absolute micro-, meso- and marco- PV (**a**) and SSA (**b**), and the percentages of micro-, meso- and marco- PV (**c**) and SSA (**d**) of transitional Longtan Shale samples from YV-1 and XD-1. The boundaries between samples of YV-1 and XD-1 are highlighted by bold dashed lines.

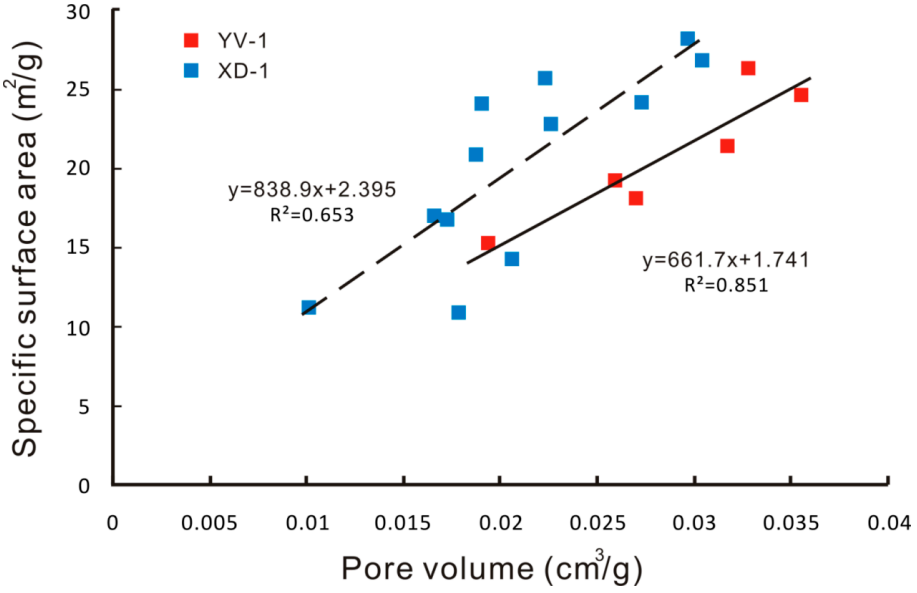

Figure 11. Relationships between pore volume and specific surface area of YV-1 and XD-1.

The distribution of pore volume with pore size can be used to represent pore size distribution, including cumulative, incremental, differential pore volume distribution curves [9]. In this study, we used incremental pore volume distribution curves to investigate the characteristic of the PSD. The peak in the PSD curve represents the development of the corresponding pore size.

It can be observed in Figure 12 that the PSD curve of shale samples is unimodal or multimodal. All samples of YV-1 exhibit the multimodality. The major peak is concentrated around 2–4 nm and the peak value can reach 0.004 cm^3/g. Other peaks are presented around 30–50 nm and the peak value can reach 0.005 cm^3/g (Figure 12a). The result showed that samples are developed fine mesopores. Samples of XD-1 are observed to be a unimodal or bimodal pattern, with the major peak is close to micropore size in the range of 0.4–1.0 nm and the secondary peak at meso- to macro-pore size range of 20–50 nm. Compared with YV-1, the main peak of XD-1 is relatively low, with the value around 0.002 cm^3/g and 0.004 cm^3/g (Figure 12b). Another great difference between samples of YV-1 and XD-1 is the different relative concentrating degree of the pores at the two peaks. Variations in relative concentrating degree may result in changes in average pore size, because one large pore can have a volume equal to many small pores [18]. Samples of YV-1 samples are relatively more enriched in large mesopores, causing it to have a larger average pore size than XD-1.

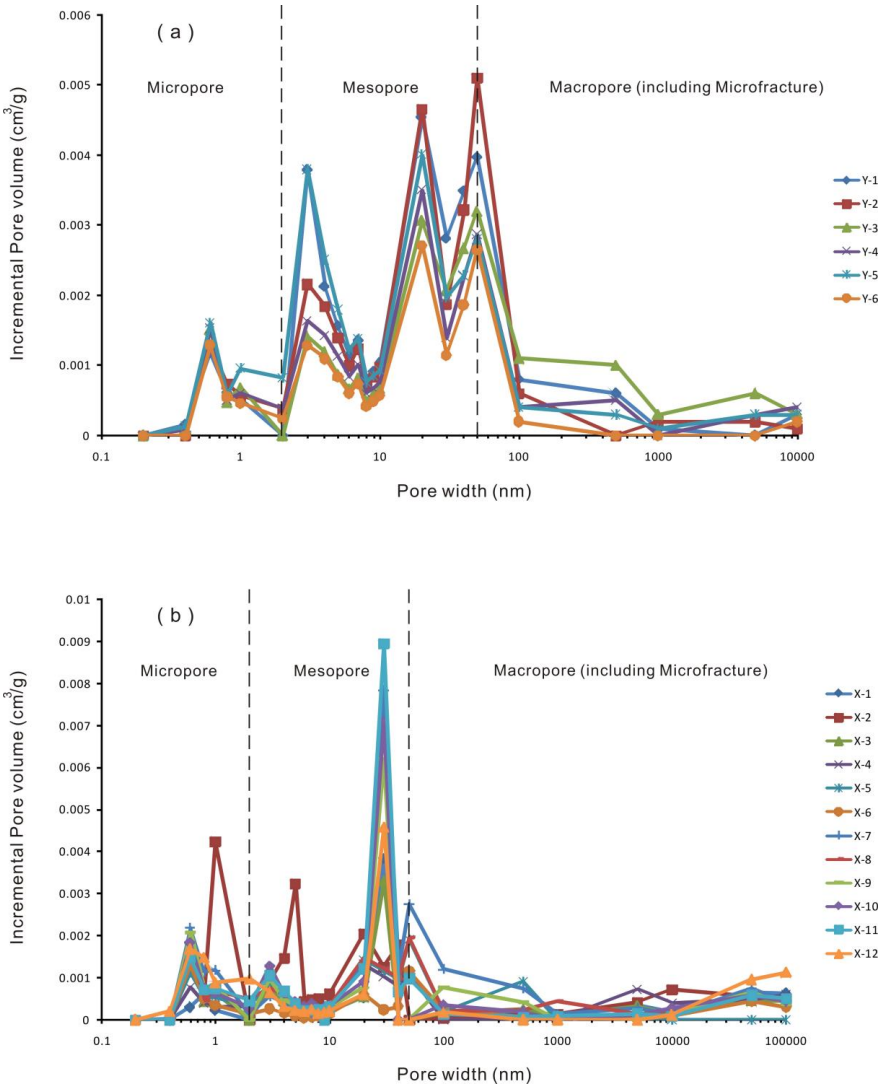

Figure 12. Pore size distribution curves of incremental pore volume of transitional Longtan Shale samples from YV-1 (**a**) and XD-1 (**b**). The boundaries between micropore, mesopore and macropore were highlighted by bold dashed lines.

4.5. Pore Morphology between Shales with Different Sedimentary Microfacies

Based on the genesis and the position within the reservoir space, pores are mainly divided into OM pores, inorganic pores (including intraparticle pores and interparticle pores), and microfractures [1]. The SEM observation and images in Figure 13 show that intraparticle pores, interparticle pores, and microfractures are well developed in the Longtan Formation Shale samples, while significant differences in OM pores between samples of YV-1 and XD-1 are observed.

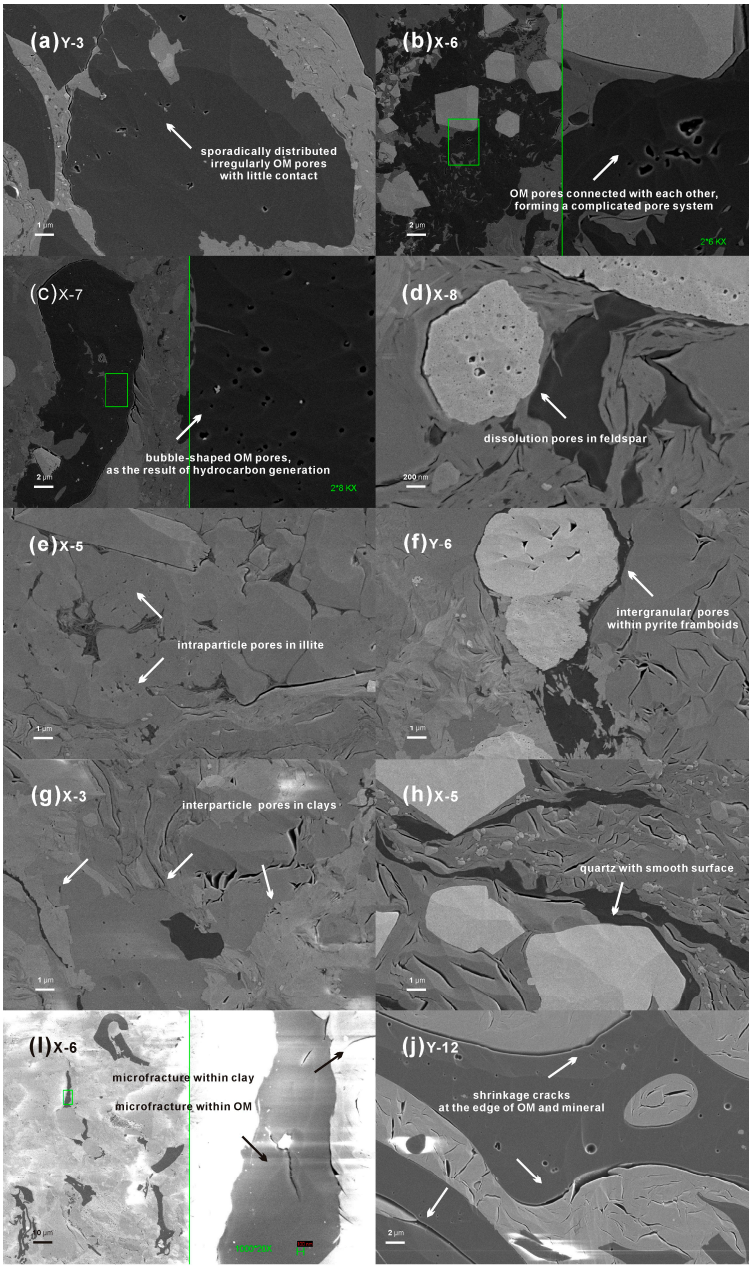

Figure 13. Scanning electron microscope (SEM) images showing major pore types of transitional Longtan Shale samples from YV-1 and XD-1. (**a**) Sporadically distributed irregularly organic matter (OM) pores with little contact; (**b**) OM pores connected with each other, forming a complicated pore system; (**c**) bubble-shaped OM pores within kerogen, as the result of hydrocarbon formation; (**d**) dissolution pores in feldspar; (**e**) intraparticle pores in illite; (**f**) intergranular pores within pyrite framboids; (**g**) interparticle pores in clays; (**h**) quartz with smooth surface; (**i**) microfractures within OM and clay; (**j**) shrinkage cracks at the edge of the OM and mineral.

OM pores result from the hydrocarbon generation with the increasing thermal maturity [57]. As shown in Figure 13a, OM pores are sporadically distributed with little contact in YV-1 samples. The rarity of OM pores can be attributed to the low maturity of OM and the type-III kerogen, which tends to generate gaseous hydrocarbons and produce only a very small amount of liquid hydrocarbons. Hence, OM pores may present limited contributions to the storage and transport of shale gas in Panxian County. OM pores were frequently observed in XD-1 samples, and some of them can be interconnected, forming an effective pore network, enhancing the heterogeneity of pore structure, and providing more reservoir space (Figure 13b). The pore geometry is mostly angular or elliptical and the pore size is in the range of 10–30 nm based on the analysis of SEM images (Figure 13c). This suggests that the OM pores in this study are mainly micropores and mesopores.

Intraparticle pores can be divided into dissolution pores, intraparticle pores within clay particles, and intergranular pores within pyrite framboids [45]. Dissolution pores are formed by the partial dissolution of particles, which is related to burial depth, pressure, temperature and acidic liquids. Dissolution pores in feldspar particles have irregular shapes and large size (Figure 13d). For the deformation of particles during compaction, intraparticle pores in illite are relatively small (Figure 13e). Intergranular pores within pyrite framboids are angular in shape and commonly found in this study (Figure 13f). Some of the pores in the pyrite framboids were filled with OM or clay minerals.

Interparticle pores are abundant in the shale samples and connect well with each other. Hence, it is an important part of the pore system, which may contribute to porosity, PV, SSA and connectivity [17,58]. Interpariticle pores occurred between clay particles are disordered lamellar, slit-shaped or wedge-shaped, and easily deformed and closed by compaction (Figure 13g). Brittle minerals, such as quartz and feldspar, can resist compaction, thereby producing some residual interparticle pores around them [18]. Most of the interparticle pores have irregular shapes and large size.

Microfractures are abundant in the shale samples, with a length of several to tens of microns and a width of several microns. Microfractures can develop in OM, clay minerals and the edge of the OM and mineral (Figure 13i). Some fractures in the clay are oriented in a certain direction by compaction. Shrinkage crack is a special kind of crack originates from the expulsion of volatile matter and the contraction of solid OM during hydrocarbon generation (Figure 13j).

5. Discussion

5.1. Contributions of Total Organic Carbon (TOC) and Mineralogical Composition to Pore Structure of Shale

The relationships between TOC content and pore structure parameters are shown in Figure 14. The positive relationships are observed between TOC content and PV (R^2 = 0.826 and 0.544 in Figure 14a), SSA (R^2 = 0.667 and 0.589 in Figure 14b), as proposed by many studies [14,56]. Both YV-1 and XD-1 have high TOC content, thus the difference may be related to their maturity. Not all OM can produce OM pores. Samples of YV-1 are in the low maturation stage, and OM pores have not yet been massively produced, which leads to a relatively low correlation. There is a significant positive relationship between TOC content and micropore volume, specific surface area (R^2 = 0.669 in Figure 14c and R^2 = 0.684 in Figure 14d) of XD-1 samples. However, we note that there is a significant positive relationship between TOC content and mesopore volume, specific surface area of YV-1 samples (R^2 = 0.668 in Figure 14e and R^2 = 0.624 in Figure 14f), rather than micropore volume and specific surface area. This difference is mainly caused by OM pores in organic matters. Bubble-shaped OM pores were frequently observed in XD-1 samples because of the formation of gaseous hydrocarbon (Figure 13c). While, irregular-shaped OM pores with the pore size in the range of 10–30 nm, which greatly contribute to mesopore volumes, were sporadically distributed in YV-1 samples based on the analysis of SEM images (Figure 13a).

The relationships between mineral composition and pore structure parameters are shown in Figure 15. The positive correlations are observed between clay minerals content and PV (R^2 = 0.930 and

0.478 in Figure 15a), SSA (R^2 = 0.903 and 0.622 in Figure 15b). Samples of YV-1 show a higher correlation because of the extremely high clay minerals content. There is a significant positive relationship between clay minerals content and mesopore volume, specific surface area (R^2 = 0.951 in Figure 15e and R^2 = 0.978 in Figure 15f) of YV-1 samples, and a positive relationship between clay minerals content and micropore volume, specific surface area of XD-1 samples (R^2 = 0.646 in Figure 15c and R^2 = 0.697 in Figure 15d). Compared with quartz and other clay minerals, the I/S has much larger specific surface area and the enrichment of the I/S can largely increase the specific surface area of shale. The large number of intraparticle pores, interparticle pores and microfractures in clay minerals (Figure 13e,h) can directly contribute to mesopore volumes, while the small holes separated by the needle-shaped minerals provide a favorable space for the development of micropores [51].

Because of brittleness, quartz content may be related to the development of microfractures [18]. However, the correlation between quartz content and pore structure in this study is not obvious. As mentioned earlier, the quartz in marine-continental transitional shale is mainly terrigenous, which contributes little to gas adsorption and has little influence on the pore structure. The SEM images also illustrate that the quartz has a smooth surface and fewer pores (Figure 13h), which could even weaken the heterogeneity of the pore structure.

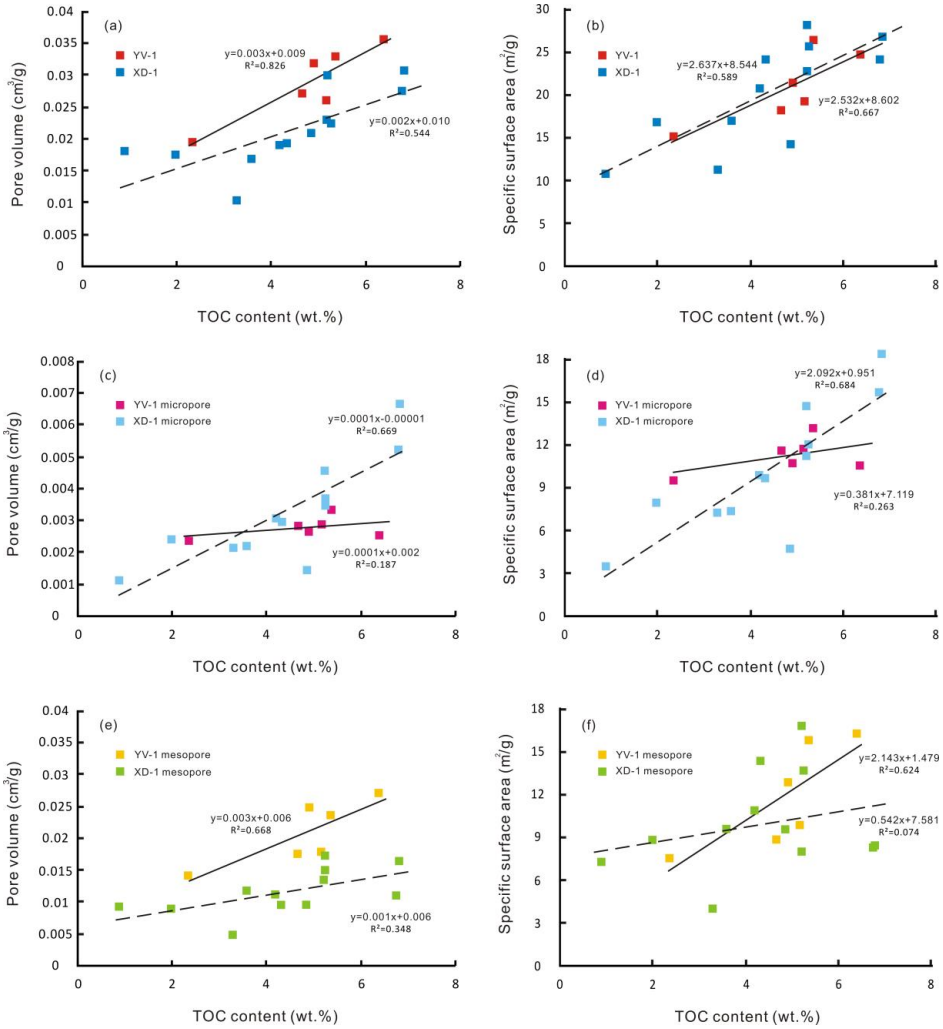

Figure 14. Relationships between TOC content and PV (**a**), SSA (**b**), micro-PV (**c**), micro-SSA (**d**), meso-PV (**e**), meso-SSA (**f**) of transitional Longtan Shale samples from YV-1 and XD-1.

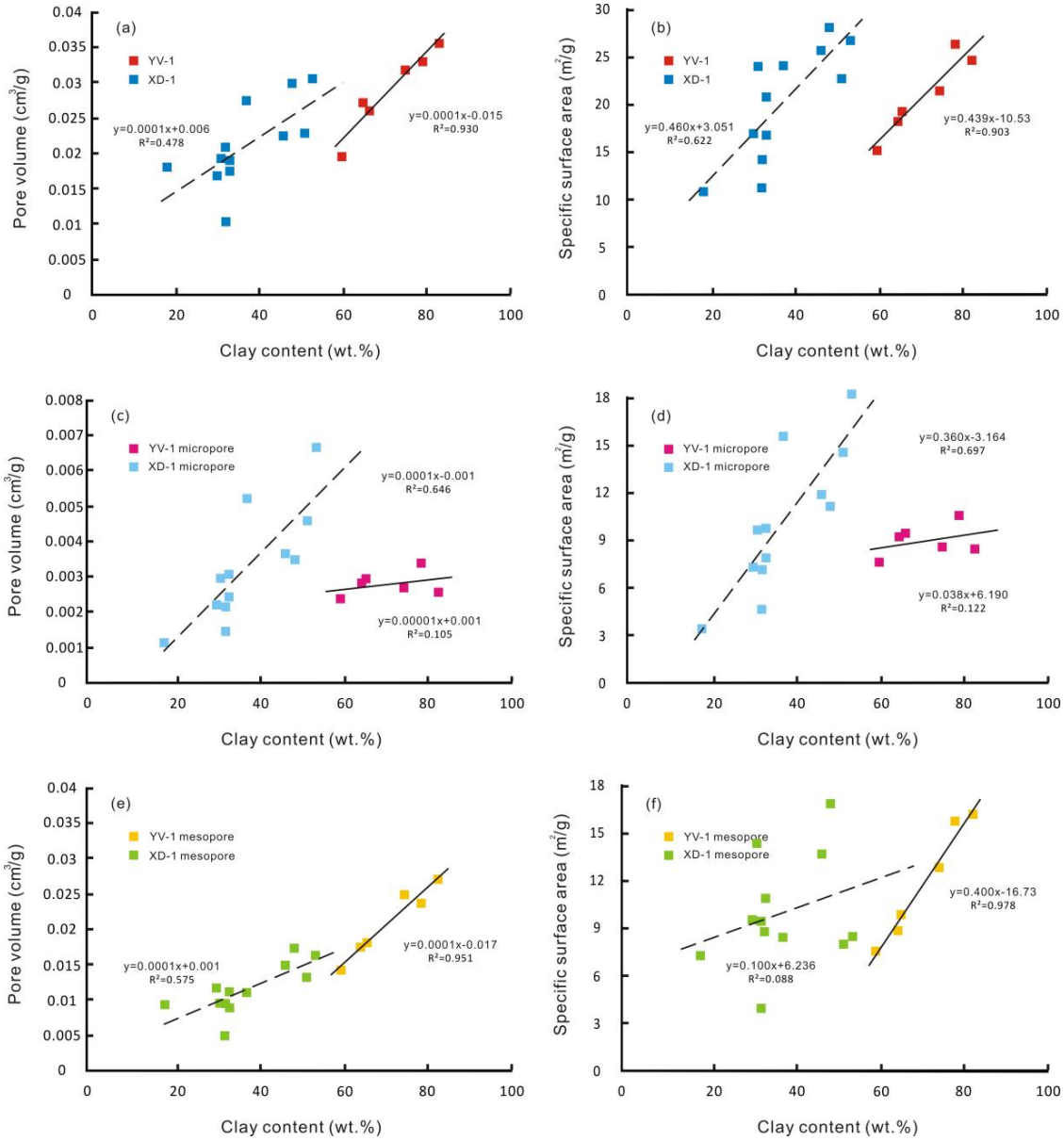

Figure 15. Relationships between clays content and PV (**a**), SSA (**b**), micro-PV (**c**), micro-SSA (**d**), meso-PV (**e**), meso-SSA (**f**) of transitional Longtan Shale samples from YV-1 and XD-1.

5.2. Relationship between TOC Content, Mineralogical Composition, Pore Structure Parameter and Fractal Dimension of Shale

The nitrogen adsorption fractal dimension (D) is positively correlated with TOC content (R^2 = 0.670 and 0.512 in Figure 16a) and clay mineral content (R^2 = 0.887 and 0.360 in Figure 16b). It suggests that TOC and clays have a significant influence on the surface roughness and the structure complexity of pore system. The irregular surface of kerogen and clay minerals enhances the heterogeneity of shale reservoir and provides more adsorption space. In addition, pore types and geometric shapes also influence fractal dimension. For example, H_2 type samples with ink bottle-shaped pores in this study have higher fractal dimensions than H_3 type samples with slit-shaped pores (Table 5 and Figure 7). As observed in SEM images, OM-hosted pores may interconnect with each other and form a complicated system during hydrocarbon generation (Figure 13b), and mineral-hosted pores may be deformed or compounded due to compaction (Figure 13g). Their properties and shapes may transform from regularity to complex and thus result in the increase of fractal dimension.

The extreme value of XD-1 in Figure 16b may originate from changes in composition or structure of clay, which leads to a relatively low correlation. As previous studies proposed [59,60], there is a negative correlation between fractal dimension and quartz content in YV-1 samples (R^2 = 0.465 in Figure 16b) and no correlation in XD-1.

The fractal dimension (D) is positively correlated with mesopore volume and specific surface area of YV-1 (R^2 = 0.916 in Figure 16e and 0.807 in Figure 16f) and micropore volume and specific surface area of XD-1 (R^2 = 0.556 in Figure 16c and 0.620 in Figure 16d). The relationships are mainly influenced by TOC content, clay content and PSD. As mentioned earlier, the PV and SSA have negative correlations with average pore diameters. Shale samples with smaller average pore diameter generally has small pores and throats, leading to a more complicated pore structure, irregular surfaces and higher fractal dimension values. However, fractal dimensions can reflect the degree of micro- and meso-pore development in such shales.

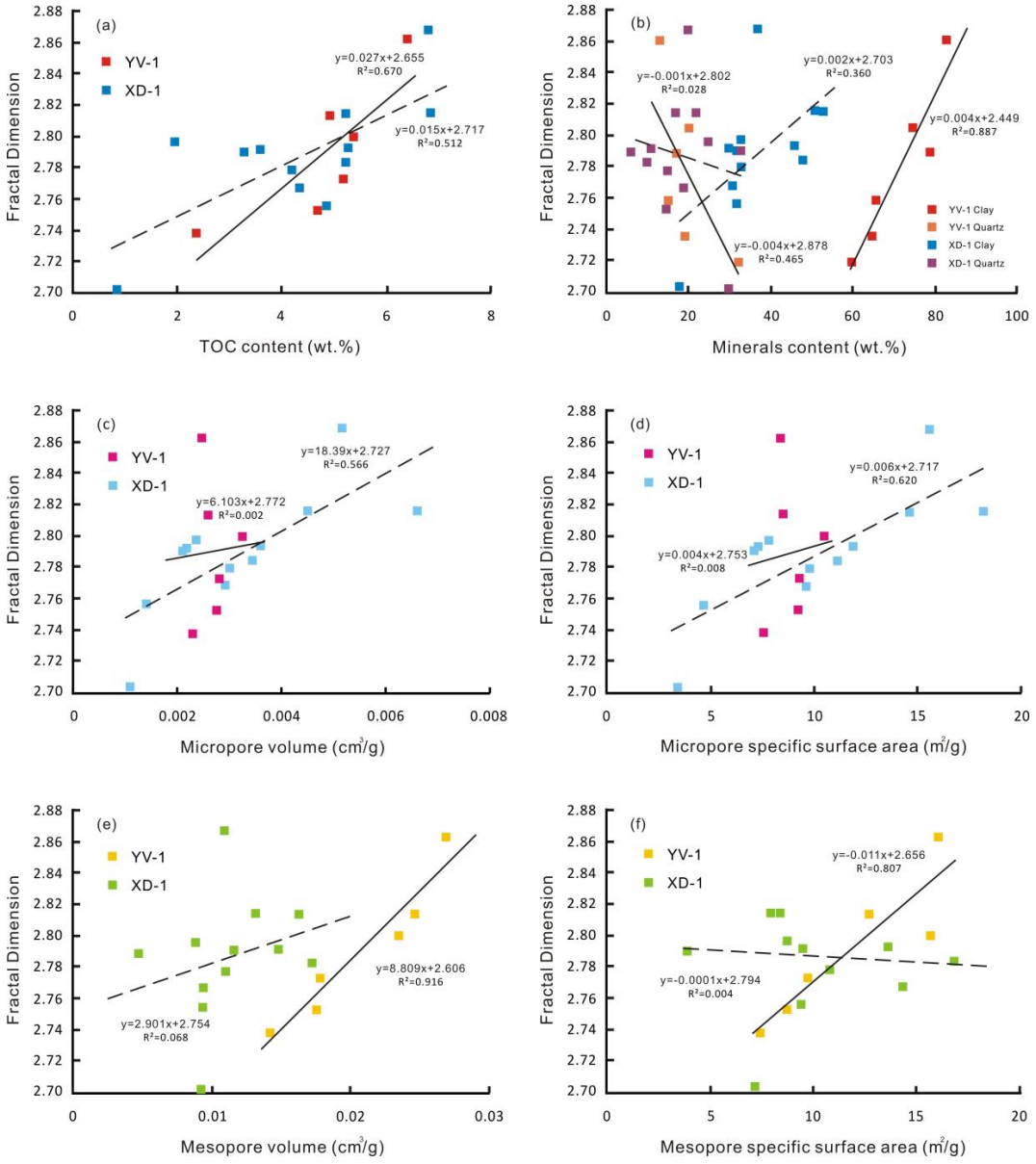

Figure 16. Relationships between fractal dimension and TOC content (**a**), clay content and quartz content (**b**), micro-PV (**c**), micro-SSA (**d**), meso-PV (**e**), meso-SSA (**f**) of transitional Longtan Shale samples from YV-1 and XD-1.

5.3. Relationship between TOC Content, Mineralogical Composition, Pore Structure Parameter and Methane Adsorption Capacity of Shale

Previous studies have shown that the gas adsorption capacity of shale is mainly related to TOC content, kerogen type, mineralogy and pore structure [15,61]. The relationships between TOC content, clay minerals content, PV, SSA and methane adsorption capacity are illustrated in Figure 17. The Langmuir volume (V_L) is positively correlated with TOC content (R^2 = 0.329 and 0.946 in Figure 17a) and clay minerals content (R^2 = 0.682 and 0.631 in Figure 17b). Kerogen is not only the material basis of hydrocarbon production, but also an important space for gas adsorption and accumulation. Previous studies [62,63] indicated that higher TOC often implies larger adsorbed gas content. Both YV-1 and XD-1 have high TOC content, thus the difference in adsorption capacity may be related to their maturity. Samples of YV-1 are in low maturation stage, and gaseous hydrocarbon has not yet been massively generated, which leads to a relatively low correlation. The rough and irregular surface of clay minerals provides abundant adsorption space. The gas adsorption capacity of various clay minerals presents the following order: I/S > kaolinite > chlorite > illite [27,64]. Samples of YV-1 have an extremely high clay minerals content with much more specific surface area, while the I/S of XD-1 samples occupies a dominant position in clay content, making a significant contribution to the rough surface and enhancing gas adsorption capacity.

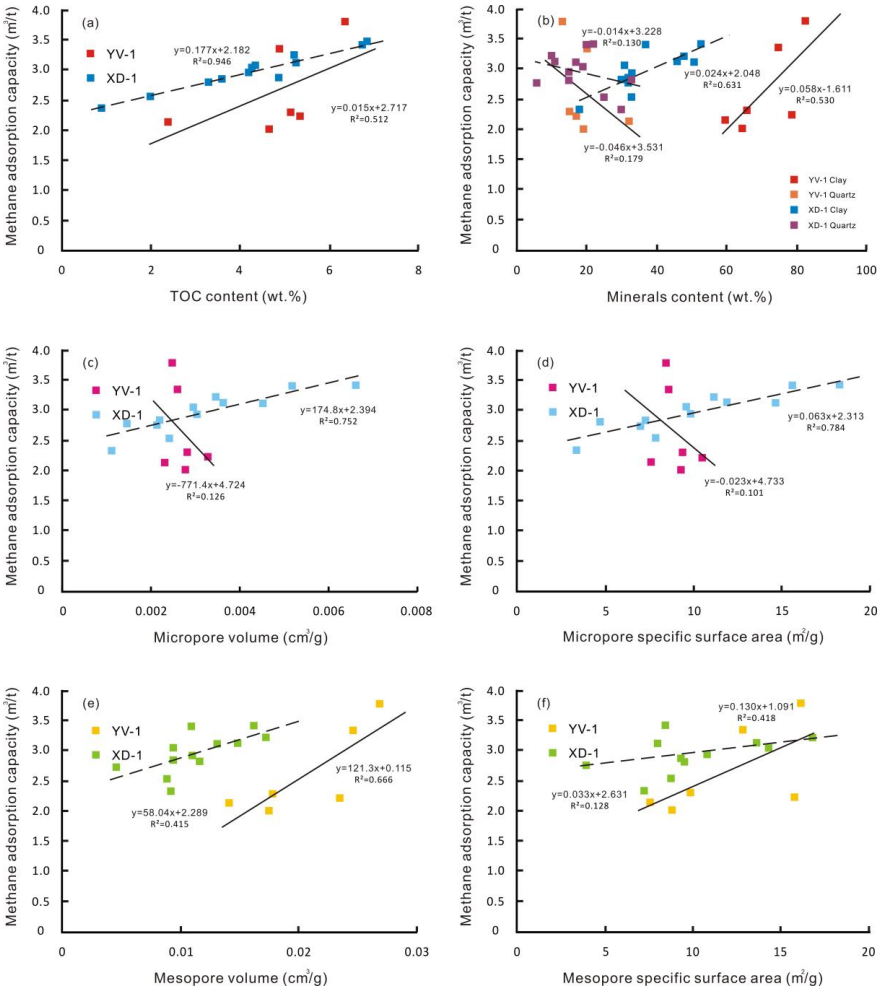

Figure 17. Relationships between methane adsorption capacity and TOC content (**a**), clay content (**b**), micro-PV (**c**), micro-SSA (**d**), meso-PV (**e**), meso-SSA (**f**) of transitional Longtan Shale samples from YV-1 and XD-1.

The Langmuir volume is positively correlated with mesopore volume and specific surface area of YV-1 (R^2 = 0.666 in Figure 17e and R^2 = 0.418 in Figure 17f), and micropore volume and specific surface area of XD-1 (R^2 = 0.752 in Figure 17c and R^2 = 0.784 in Figure 17d). However, some previous research suggested that micropore is the important control on gas adsorption, while mesopore and macropore are do not appear to affect the gas adsorption and instead to be the gas transport pathways [56]. Sun et al. [53] suggested that mesopore volume can also contribute to gas adsorption. The reasons for these phenomena are different. In this study, in addition to the effect of TOC and clays on PV and SSA, the result could be related to the pore composition. In YV-1 samples, mesopore occupies an absolute advantage and contributes to gas adsorption capacity, while, in XD-1 samples, besides mesopores, micropores also occupy a certain proportion, which can affect the gas adsorption capacity (Figure 10c). Moreover, the PV and SSA have negative correlations with average pore diameters. The smaller pore diameter leads to a greater adsorption interaction between gas molecules and pore surface [49] and results in a stronger adsorption potential energy, which enhances the adsorption capacity of a shale gas reservoir.

5.4. Comparison of TOC Content, Mineralogical Composition and Pore Structure Parameters between Shales with Different Sedimentary Microfacies

The YV-1 well is located in a coal-bearing basin in Panxian County and presents a transitional facies dominated by delta and lower delta plains environments. The XD-1 well is located in a smooth syncline in Xingren County and presents a transitional facies dominated by lagoon-tidal flat environments (Figures 1 and 2). In XD-1, the whole suite of coal-bearing sequences is dominated by fine-grained sediments, which mainly consists of silty mudstone, carbonaceous shale, siliceous shale and coal seam. While, in YV-1, the turbulent depositional environment caused dark mudstones frequently interbedded with silty mudstone, carbonaceous mudstone and coal seam, showing a more complex lithological assemblage in the vertical direction. As shown in Table 7, both the thickness of Longtan Formation and the thickness of organic-rich shale of XD-1 are larger than those of YV-1.

Samples of YV-1 and XD-1 have similar TOC content (on average 4.82% and 4.38%, respectively). The high TOC content may be related to the presence of coal-bearing sequences in the study areas. As mentioned previously, YV-1 samples are low matured and thermal maturity has been in the oil window, while XD-1 samples are over matured and thermal maturity has been in the dry-gas window. As shown in Table 7, mineralogical composition is significantly different in two wells. Samples of YV-1 have an extreme high content of clay mineral (71.33% average) and clay mineral is mainly consist of the I/S, chlorite and kaolinite (on average 41.67%, 29.33% and 26%, respectively), while samples of XD-1 have a relatively low clay mineral content (37% average) and the I/S occupies an absolute advantage (61.33% average), leaving the content of kaolinite and chlorite is less than 10%. The average PV, SSA and average pore diameter values of YV-1 are larger than those of XD-1 (Table 7), and mesopore occupies an absolute advantage, which contributes to a greater gas adsorption and storage potential. The fractal dimension value of XD-1is slightly larger than that of YV-1 (on average 2.787 and 2.756, respectively), indicating a more rough surface and a more complicated structure of shale reservoir. OM pores are more developed in XD-1 and the pore type can be divided into type H_2 hysteresis, which indicates ink bottle-shaped pores. Samples of YV-1 can be mainly classified as typeH_3 hysteresis, which indicates slit-shaped pores and wedge-shaped pores. Compared with XD-1, the relationship between fractal dimension, methane adsorption capacity and pore structure parameters for mesopore is more obvious than for micropore in YV-1, which is mainly related to the effect of TOC content, mineral composition and pore size distribution.

However, differences in TOC content, mineral composition and pore structure mentioned above may be related to depositional environment and material sources. Nevertheless, porosity characteristic of studied shales could also be effected by burial depth and regional tectonic movements. Therefore, this possible impact should be studied in future.

Table 7. Organic geochemical characteristic, mineralogical composition and pore structure parameters of transitional Longtan Shale samples from YV-1 and XD-1.

Sample	YV-1	XD-1
Sedimentary microfacies	delta and lower delta plains	lagoon-tidal flat
Lithology	dark mudstone interbedded silty mudstone, carbonaceous mudstone and coal seam	dark shale interbedded with silty mudstone, carbonaceous shale, siliceous shale and coal seam
Thickness of Longtan Formation (m)	170–300	260–380
Cumulative thickness of shale (m)	40–60	40–100
TOC (wt.%)	2.36–6.40/4.82	0.89–6.85/4.38
R_o (%)	0.86–1.17/1.06	2.50–2.93/2.69
δ^{13} C (‰)	−24.9~−23.4	−24.6~−23.2
Kerogen Type	III	III
Clay mineral content (wt.%)	60–83/71.33	18–53/37.00
Brittle mineral content (wt.%)	13–40/27.50	13–47/30.25
I/S content (wt.%)	27–60/41.67	39–79/61.33
Porosity (%)	0.91–2.44/1.69	0.87–3.42/1.82
Permeability (10^{-5} mD)	0.20–1.25/0.49	0.003–1.917/0.28
Langmuir volume (m^3/t)	2.02–3.78/2.64	2.34–3.41/2.96
Micropore volume (cm^3/g)	0.00230–0.00328/0.00271	0.00113–0.00663/0.00320
Mesopore volume (cm^3/g)	0.00142–0.02688/0.02077	0.00477–0.01720/0.01136
Macropore volume (cm^3/g)	0.0030–0.0068/0.0053	0.0029–0.0112/0.0065
Total Pore volume (cm^3/g)	0.01948–0.03556/0.02881	0.01021–0.03043/0.02110
Micropore surface area (m^2/g)	7.603–10.528/8.9595	3.402–18.279/10.1204
Mesopore surface area (m^2/g)	7.544–16.131/11.8084	3.952–16.823/9.9588
Macropore surface area (m^2/g)	0.014–0.071/0.0383	0.002–0.077/0.0209
Total surface area (m^2/g)	15.161–26.315/20.806	10.668–28.021/20.101
Average pore diameter (nm)	9.99–11.95/11.07	6.39–13.42/8.40
Fractal dimension	2.625–2.862/2.756	2.702–2.867/2.787

6. Conclusions

In this paper, organic geochemical characteristic, mineralogical composition, pore structure and fractal characteristic of the marine-continental transitional facies Longtan Formation Shale in the southwest of Guizhou Province were investigated using organic petrography analysis, XRD analysis, FE-SEM analysis, the NMR test, MICP and gas adsorption experiments. Relationships among TOC contents, mineral compositions, pore structure parameters, methane adsorption capacity and fractal dimensions were discussed, along with the differences between different sedimentary microfacies. Our main conclusions are summarized as follows:

1. Shales in this study were collected from the YV-1 well in Panxian County and the XD-1 well in Xingren County. They present the transitional environment dominated by delta and lower delta plains, and the transitional environment dominated by lagoon-tidal flat, respectively. In YV-1, the turbulent depositional environment caused dark mudstones frequently interbedded with other fine-grained sediments, showing a more complex lithological assemblage in the vertical direction.
2. Shale samples of YV-1 and XD-1 are characterized by high TOC contents (on average 4.82% and 4.38%), low permeability (on average 0.49×10^{-5} mD and 0.28×10^{-5} mD) and complex mineral composition. Samples of YV-1 have an extreme high content of clay mineral (71.33% average) and clay mineral is mainly consist of the I/S, chlorite and kaolinite. While, samples of XD-1 have a relatively low clay mineral content (37% average) and the I/S occupies an absolute advantage. These differences may be related to the depositional environments and material sources. The average PV and SSA values of YV-1 are larger than those of XD-1, indicating a greater gas adsorption and storage potential. Samples of YV-1 have multimodal PSD curves with the major peak at 40–50 nm, which suggests that mesopore occupies an absolute advantage and is the predominant contributor to pore structure. Samples of XD-1 have bimodal PSD curves

with a major peak at 3–4 nm, which indicates that micropore also occupies a certain proportion in addition to mesopore.

3. Samples have the same kerogen type (type III) and different maturity. OM pores are largely developed in XD-1 samples, whose kerogen is in the stage of dry gas window. Clay mineral-hosted pores, including intraparticle pores and interparticle pores, dominate the pore system of YV-1. According to the type of hysteresis loops, pore geometries of YV-1 and XD-1 are mainly slit-shaped (type H_3 hysteresis) and ink bottle-shaped (type H_2 hysteresis), respectively. The fractal dimension value of XD-1is slightly larger than that of YV-1 (on average 2.787 and 2.756), indicating a rougher surface and a more complicated structure of shale reservoir. The gas adsorption capacity is mainly affected by the TOC contents, clay mineral compositions and pore SSA, and has a significant positive correlation with fractal dimension value.
4. Based on the comprehensive comparison of geological characteristic, organic geochemical characteristic, mineralogical composition, pore structure, gas adsorption capacity and fractal characteristic of YV-1 and XD-1, it is clear that shales deposited in a lagoon-tidal flat environment with high TOC content, higher maturity, suitable clay mineral contents and quartz contents, high PV and SSA, and higher fractal dimension have a greater potential for shale gas development.

Author Contributions: X.M. participated in all data and figures processing, and wrote the original manuscript. S.G. put forward the concept and was responsible for project administration, supervision and validation. All authors participated in writing the manuscript.

Funding: This research is a part of the research of Study on Formation Mechanism and Enrichment Regularity of Different Types of Shale Gas, which is financially supported by the National Science and Technology Major Project of the Ministry of Science and Technology of China (No. 2016ZX05034-001).

Acknowledgments: We would like to thank all editors and reviewers for their constructive comments on this paper.

Conflicts of Interest: The authors declare no conflict of interest.

References

1. Loucks, R.G.; Reed, R.M.; Ruppel, S.C.; Jarvie, D.M. Morphology, genesis and distribution of nanometer-scale pores in siliceous mudstones of the Mississippian Barnett Shale. *J. Sediment. Res.* **2009**, *79*, 848–861. [CrossRef]
2. IUPAC (International Union of Pure and Applied Chemistry). Physical Chemistry Division Commission on Colloid and Surface Chemistry, Subcommittee on Characterization of Porous Solids: Recommendations for the characterization of porous solids (Technical Report). *Pure Appl. Chem.* **1994**, *66*, 1739–1758. [CrossRef]
3. Clarkson, C.R.; Solano, N.; Bustin, R.M.; Bustin, A.M.M.; Chalmers, G.R.L.; Hec, L. Pore structure characterization of North American shale gas reservoirs using USANS/SANS, gas adsorption and mercury intrusion. *Fuel* **2013**, *103*, 606–616. [CrossRef]
4. Curtis, M.E.; Ambrose, R.J.; Sondergeld, C.H.; Rai, C.S. Microstructural investigation of gas shales in two and three dimensions using nanometer-scale resolution imaging. *AAPG Bull.* **2012**, *96*, 665–677. [CrossRef]
5. Bernard, S.; Horsfield, B.; Schulz, H.M.; Wirth, R.; Schreiber, A.; Sherwood, N. Geochemical evolution of organic-rich shales with increasing maturity: A STXM and TEM study of the Posidonia Shale (Lower Toarcian, northern Germany). *Mar. Pet. Geol.* **2012**, *31*, 70–89. [CrossRef]
6. Houben, M.; Desbois, G.; Urai, J. Pore morphology and distribution in the Shaly facies of Opalinus Clay: Insights from representative 2D BIB-SEM investigations on mm to nm scale. *Appl. Clay Sci.* **2013**, *71*, 82–97. [CrossRef]
7. Keller, L.M.; Schuetz, P.; Erni, R.; Rossell, M.D.; Lucas, F.; Gasser, P.; Holzer, L. Characterization of multi-scale microstructural features in Opalinus Clay. *Microporous Mesoporous Mater.* **2013**, *170*, 83–94. [CrossRef]
8. Chalmers, G.R.L.; Bustin, R.M.; Power, I.M. Characterization of gas shale pore systems by porosimetry, pycnometry, surface area, and field emission scanning electron/transmission electron microscopy image analyses: Examples from the Barnett Woodford, Haynesville, Marcellus and Doig units. *AAPG Bull.* **2012**, *96*, 1099–1119. [CrossRef]

9. Tian, H.; Pan, L.; Xiao, X.; Wilkins, R.W.; Meng, Z.; Huang, B. A preliminary study on the pore characterization of lower Silurian black shales in the Chuandong thrust fold belt, southwestern China using low pressure N_2 adsorption and FE-SEM methods. *Mar. Pet. Geol.* **2013**, *48*, 8–19. [CrossRef]
10. Yang, C.; Zhang, J.C.; Tang, X.; Ding, J.H.; Zhao, Q.R.; Dang, W.; Chen, H.Y.; Su, Y.; Li, B.W.; Lu, D.F. Comparative study on micro-pore structure of marine, terrestrial, and transitional shales in key areas, China. *Int. J. Coal Geol.* **2017**, *171*, 76–92. [CrossRef]
11. Mandelbrot, B.B. *Les Objects Fractals: Forme, Hasard et Dimension*; Flammarion: Paris, France, 1984.
12. Avnir, D.; Jaroniec, M. An isotherm equation for adsorption on fractal surfaces of heterogeneous porous materials. *Langmuir* **1989**, *5*, 1412–1433. [CrossRef]
13. Yao, Y.B.; Liu, D.M.; Che, Y.; Tang, D.Z.; Tang, S.H.; Huang, W.H. Petrophysical characterization of coals by low-field nuclear magnetic resonance (NMR). *Fuel* **2010**, *89*, 1371–1380. [CrossRef]
14. Hu, J.G.; Tang, S.H.; Zhang, S.H. Investigation of pore structure and fractal characteristics of the Lower Silurian Longmaxi shales in western Hunan and Hubei Provinces in China. *J. Nat. Gas Sci. Eng.* **2016**, *28*, 522–535. [CrossRef]
15. Chalmers, G.R.L.; Bustin, R.M. Lower Cretaceous gas shales in northeastern British Columbia: Part I. Geological controls on methane sorption capacity. *Bull. Canad. Pet. Geol.* **2008**, *56*, 1–21. [CrossRef]
16. Lin, L.; Zhang, J.; Li, Y.; Jiang, S.; Tang, X.; Jiang, S.; Jiang, W. The potential of China's lacustrine shale gas resources. *Energy Explor. Exploit.* **2013**, *31*, 317–335. [CrossRef]
17. Jiao, K.; Yao, S.; Liu, C.; Gao, Y.; Wu, H.; Li, M.; Tang, Z. The characterization and quantitative analysis of nanopores in unconventional gas reservoirs utilizing FESEM–FIB and image processing: An example from the lower Silurian Longmaxi Shale, upper Yangtze region, China. *Int. J. Coal Geol.* **2014**, *128–129*, 1–11. [CrossRef]
18. Xi, Z.D.; Tang, S.H.; Zhang, S.H.; Li, J. Nano-Scale Pore Structure of Marine-Continental Transitional Shale from Liulin Area, the Eastern Margin of Ordos Basin, China. *J. Nanosci. Nanotechnol.* **2017**, *17*, 6109–6123. [CrossRef]
19. Yang, F.; Ning, Z.F.; Hu, C.P.; Wang, B.; Peng, K.; Liu, H.Q. Characterization of microscopic pore structures in shale reservoirs. *J. Acta Pet. Sin.* **2013**, *34*, 301–311.
20. Gai, S.H.; Liu, H.Q.; He, S.N.; Mo, S.Y.; Chen, S.; Liu, R.H.; Huang, X.; Tian, J.; Lv, X.C.; Wu, D.X. Shale reservoir characteristics and exploration potential in the target: A case study in the Longmaxi Formation from the southern Sichuan Basin of China. *J. Nat. Gas Sci. Eng.* **2016**, *31*, 86–97. [CrossRef]
21. Gao, J.; Liu, G.D.; Yang, W.W.; Zhao, D.R.; Chen, W.; Liu, L. Geological and geochemical characterization of lacustrine shale, a case study of Lower Jurassic Badaowan shale in the Junggar Basin, Northwest China. *J. Nat. Gas Sci. Eng.* **2016**, *31*, 15–27. [CrossRef]
22. Sun, M.; Yu, B.; Hu, Q.; Chen, S.; Xia, W.; Ye, R. Nanoscale pore characteristics of the lower Cambrian Niutitang formation shale: A case study from Well Yuke #1 in the southeast of Chongqing, China. *Int. J. Coal Geol.* **2016**, *154*, 16–29.
23. Wu, H.; Yao, S.; Jiao, K. Shale gas exploration prospect of Longtan Formation in the Lower Yangtze area of China. *J. China Coal Soc.* **2013**, *38*, 870–876.
24. Yan, D.; Huang, W.H.; Lu, X.X. Contrast of reservoir forming conditions of marine-continental transitional shale gas in different sedimentary environments in the Lower Yangtze area of China. *J. China Coal Soc.* **2016**, *417*, 1778–1787.
25. Guo, S.B.; Fu, J.J.; Gao, D. Research status and prospects for marine-continental shale gas in China. *Pet. Geol. Exp.* **2015**, *37*, 353–540.
26. Niu, X.S.; Feng, C.M.; Liu, J. Formation mechanism and time of Qianzhong uplift. *Mar. Orig. Petrol. Geol.* **2007**, *12*, 46–50.
27. Li, A.; Ding, W.L.; Jiu, K.; Wang, Z.; Wang, R.Y.; He, J.H. Investigation of the pore structures and fractal characteristics of marine shale reservoirs using NMR experiments and image analyses: A case study of the Lower Cambrian Niutitang Formation in northern Guizhou Province, South China. *Mar. Pet. Geol.* **2018**, *89*, 530–540. [CrossRef]
28. Xiao, K. Analysis of principles for geological structures of Yueliangtian Coal Mine. *Min. Saf. Environ. Prot.* **2003**, *30*, 25–26.
29. Dou, X.Z.; Jiang, B.; Qin, Y.; Wang, W.; Chen, W.Y. Structure Evolution in West of Guizhou Area and Control to Seam in Late Permian. *Coal Sci. Technol.* **2012**, *40*, 109–114.

30. Gu, C.L. Geological characteristics and prospect evaluation on coal-seam gas in East Yunnan and West Guizhou area. *XinJiang Pet. Geol.* **2002**, *23*, 106–110.
31. Dai, S.F.; Ren, D.Y.; Tang, Y.G.; Yue, M.; Hao, L.M. Concentration and distribution of elements in Late Permian coals from western Guizhou Province, China. *Int. J. Coal Geol.* **2005**, *61*, 119–137. [CrossRef]
32. Zhang, T.W.; Ellis, G.S.; Rupple, S.C.; Milliken, K.; Yang, R. Effect of organic matter type and thermal maturity on methane adsorption in shale-gas systems. *Org. Geochem.* **2012**, *47*, 120–131. [CrossRef]
33. Bustin, R.M.; Bustin, A.M.M.; Cui, X.; Ross, D.J.K.; Murthy, P.V.S. Impact of shale properties on pore structure and storage characteristics. In Proceedings of the Shale Gas Production Conference, Fort Worth, TX, USA, 16–18 November 2008.
34. Washburn, E.W. Note on a method of determining the distribution of pore sizes in a porous material. *Proc. Natl. Acad. Sci. USA* **1921**, *7*, 115–116. [CrossRef] [PubMed]
35. Barrett, E.P.; Joyner, L.G.; Halenda, P.P. The determination of pore volume and area distribution in porous substances: Computations from nitrogen isotherms. *J. Am. Chem. Soc.* **1951**, *73*, 373–380. [CrossRef]
36. Webb, P.A.; Orr, C. *Analytical Methods in Fine Particle Technology*; Micromeritics Instrument: Norcross, GA, USA, 1997.
37. Liu, Y.; Wilcox, J. Molecular simulation of CO_2 adsorption in micro- and mesoporous carbons with surface heterogeneity. *Int. J. Coal Geol.* **2012**, *104*, 83–95. [CrossRef]
38. Karayiğit, A.İ.; Mastalerz, M.; Oskay, R.G.; Buzkan, İ. Bituminous coal seams from underground mines in the Zonguldak Basin (NW Turkey): Insights from mineralogy, coal petrography, Rock-Eval pyrolysis, and meso- and microporosity. *Int. J. Coal Geol.* **2018**, *199*, 91–122. [CrossRef]
39. Mastalerz, M.; He, L.; Melnichenko, Y.B.; Rupp, J.A. Porosity of coal and shale: Insights from gas adsorption and SANS/USANS techniques. *Energy Fuels* **2012**, *26*, 5109–5120. [CrossRef]
40. Weniger, P.; Kalkreuth, W.; Busch, A.; Krooss, B.M. High-pressure methane and carbon dioxide sorption on coal and shale samples from the Paraná Basin, Brazil. *Int. J. Coal Geol.* **2010**, *84*, 109–205. [CrossRef]
41. Zou, C.N.; Dong, D.Z.; Wang, S.J.; Li, J.Z.; Li, X.J.; Wang, Y.M.; Li, D.H.; Chen, K.M. Geological characteristics, formation mechanism and resource potential of shale gas in China. *Pet. Explor. Dev.* **2010**, *37*, 641–653. [CrossRef]
42. Tissot, B.; Durand, B.; Espitalie, J.; Combaz, A. Influence of nature and diagenesis of organic matter in formation of petroleum. *AAPG Bull.* **1974**, *58*, 499–506.
43. Rimmer, S.M.; Davis, A. The influence of depositional environments on coal petrographic composition of the Lower Kittaning Seam, western Pennsylvania. *Org. Geochem.* **1988**, *12*, 375–387. [CrossRef]
44. Bustin, R.M.; Bustin, A.; Ross, D.; Chalmers, G.; Murthy, V.; Laxmi, C.; Cui, X. Shale gas opportunities and challenges. *Search Discov.* **2009**, *40*, 20–23.
45. Luo, W.; Hou, M.C.; Liu, X.C.; Huang, S.G.; Chao, H.; Zhang, R.; Deng, X. Geological and geochemical characteristics of marine-continental transitional shale from the Upper Permain Longtan formation, Northwestern Guizhou, China. *Mar. Pet. Geol.* **2018**, *89*, 58–67. [CrossRef]
46. Passey, Q.R.; Bohacs, K.; Esch, W.L.; Klimentidis, R.; Sinha, S. From oil-prone source rock to gas-producing shale reservoir-Geologic and petrophysical characterization of unconventional shale-gas reservoirs. In Proceedings of the International Oil and Gas Conference and Exhibition, Beijing, China, 8–10 June 2010.
47. Guo, S.B.; Wang, F.T.; Mao, W.J.; Peng, Y.X. Evolution of Clay Mineral and the Division of Diagenesis Stages in Mud Shale Based on Thermal Simulation. *Sci. Technol. Eng.* **2018**, *18*, 174–179.
48. Nie, H.S.; Tang, X.; Bian, R. Controlling factors for shale gas accumulation and prediction of potential development area in shale gas reservoir of South China. *Acta Pet. Sin.* **2009**, *30*, 484–490.
49. Gregg, S.J.; Sing, K.S.W. *Adsorption, Surface Area, and Porosity*; Academic Press: New York, NY, USA, 1982.
50. Sing, K.S.W.; Everett, D.H.; Haul, R.A.W.; Moscou, L.; Pierotti, R.A.; Rouquerol, J.; Siemieniewska, T. Reporting physisorption data for gas/solid systems with special reference to the determination of surface area and porosity. *Pure Appl. Chem.* **1985**, *57*, 603–619. [CrossRef]
51. Kuila, U.; Prasad, M. Specific surface area and pore-size distribution in clays and shale. *Geophys. Prospect.* **2013**, *61*, 341–362. [CrossRef]
52. Tang, X.; Jiang, Z.; Li, Z.; Gao, Z.; Bai, Y.; Zhao, S.; Feng, J. The effect of the variation in material composition on the heterogeneous pore structure of high-maturity shale of the Silurian Longmaxi formation in the southeastern Sichuan Basin, China. *J. Nat. Gas Sci. Eng.* **2015**, *23*, 464–473. [CrossRef]

53. Sun, Y.S.; Guo, S.B. Characterization of Whole-Aperture Pore Structure and Its Effect on Methane Adsorption Capacity for Transitional Shales. *Energy Fuels* **2016**, *31*, 751–763. [CrossRef]
54. Dollimore, D.; Heal, G.R. An improved method for the calculation of pore-size distribution from adsorption data. *J. Appl. Chem.* **1964**, *14*, 109–114. [CrossRef]
55. Valenza, J.J.; Drenzek, N.; Marques, F.; Pagels, M.; Mastalerz, M. Geochemical controls on shale microstructure. *Geology* **2013**, *41*, 611–614. [CrossRef]
56. Yang, F.; Ning, Z.F.; Liu, H. Fractal characteristics of shales from a shale gas reservoir in the Sichuan Basin, China. *Fuel* **2014**, *115*, 378–384. [CrossRef]
57. Mastalerz, M.; Schimmelmann, A.; Drobniak, A.; Chen, Y. Porosity of Devonian and Mississippian New Albany Shale across a maturation gradient: Insights from organic petrology, gas adsorption, and mercury intrusion. *AAPG Bull.* **2013**, *97*, 1621–1643. [CrossRef]
58. Fishman, N.S.; Hackley, P.C.; Lowers, H.A.; Hill, R.J.; Blum, A.E. The nature of porosity in organic-rich mudstones of the Upper Jurassic Kimmeridge Clay Formation, North Sea, offshore United Kingdom. *Int. J. Coal Geol.* **2012**, *103*, 32–50. [CrossRef]
59. Wang, M.; Xue, H.T.; Tian, S.S.; Wilkins, R.W.T.; Wang, Z.W. Fractal characteristics of upper cretaceous lacustrine shale from the songliao basin, NE China. *Mar. Pet. Geol.* **2015**, *67*, 144–153. [CrossRef]
60. Li, A.; Ding, W.L.; He, J.H.; Dai, P.; Yin, S.; Xie, F. Investigation of pore structure and fractal characteristics of organic-rich shale reservoirs: A case study of Lower Cambrian Qiongzhusi formation in Malong block of eastern Yunnan Province, South China. *Mar. Pet. Geol.* **2016**, *70*, 46–57. [CrossRef]
61. Ross, D.J.K.; Bustin, R.M. The importance of shale composition and pore structure upon gas storage potential of shale gas reservoirs. *Mar. Pet. Geol.* **2009**, *26*, 916–927. [CrossRef]
62. Zhou, S.D.; Liu, D.M.; Cai, Y.D.; Yao, Y.B. Fractal characterization of pore-fracture in low-rank coals using a low-field NMR relaxation method. *Fuel* **2016**, *181*, 218–226. [CrossRef]
63. Lin, T.; Duan, W.Z.; Ren, H.J.; Lu, X.X. The formation and evolution of shale pore space and pore effects to gas bearing capacity. *Chin. J. Geol.* **2017**, *52*, 141–155.
64. Ji, L.M.; Zhang, T.W.; Milliken, K.L.; Qu, J.L.; Zhong, X.L. Experimental investigation of main controls to methane adsorption in clay-rich rocks. *Appl. Geochem.* **2012**, *27*, 2533–2545. [CrossRef]